





Simulating fluorine *K*-edge resonant inelastic x-ray scattering of sulfur hexafluoride and the effect of dissociative dynamics

Ambar Banerjee ^{1,2,*}, Vinícius Vaz da Cruz,^{3,*} Victor Ekholm,⁴ Conny Sâthe,⁴ Jan-Erik Rubensson ²,
Nina Ignatova ⁵, Faris Gel'mukhanov,^{5,3} and Michael Odelius ^{1,†}

¹*Department of Physics, Stockholm University, AlbaNova University Center, SE-106 91 Stockholm, Sweden*

²*Department of Physics and Astronomy, X-ray Photon Science, Uppsala University, Ångströmlaboratoriet, Lägerhyddsvägen 1, 75120 Uppsala, Sweden*

³*Institute Methods and Instrumentation for Synchrotron Radiation Research, Helmholtz Center Berlin for Materials and Energy, 12489 Berlin, Germany*

⁴*MAX IV Laboratory, Lund University, SE-221 00 Lund, Sweden*

⁵*Theoretical Chemistry and Biology, Royal Institute of Technology, S-106 91 Stockholm, Sweden*



(Received 26 April 2023; accepted 14 July 2023; published 2 August 2023)

We report on a computational study of resonant inelastic x-ray scattering (RIXS), at different fluorine *K*-edge resonances of the SF₆ molecule, and corresponding nonresonant x-ray emission. Previously measured polarization dependence in RIXS is reproduced and traced back to the local σ and π symmetry of the molecular orbitals and corresponding states involved in the RIXS process. Also electron-hole coupling energies are calculated and related to experimentally observed spectator shifts. The role of dissociative S-F bond dynamics is explored to model detuning of RIXS spectra at the |F1s⁻¹6a_{1g}¹_g) resonance, which shows challenges to accurately reproduce the required steepness for core-excited potential energy surface. We show that the RIXS spectra can only be properly described by considering breaking of the global inversion symmetry of the electronic wave function and core-hole localization, induced by vibronic coupling. Due to the core-hole localization we have symmetry forbidden transitions, which lead to additional resonances and changing width of the RIXS profile.

DOI: [10.1103/PhysRevA.108.023103](https://doi.org/10.1103/PhysRevA.108.023103)

I. INTRODUCTION

Several techniques in x-ray spectroscopy have emerged as powerful tools for analyzing molecular and electronic structure, and dynamics [1,2]. In particular, resonant inelastic x-ray scattering (RIXS) and x-ray emission (XE) spectroscopy have been forerunners in the investigation of a gamut of chemical systems in both gas and condensed phases [3–5]. For light elements, fluorescence decay is a minority channel in relation to Auger decay, but it is more readily associated with a molecular orbital analysis. Hence, the emitted photons give a rich probe containing convoluted information about structural, electronic, and dynamical degrees of freedom [6]. The RIXS technique has revealed precise quantum mechanical effects at play at the molecular level and has been used to accurately probe photophysical and photochemical processes even at the ultrafast regime [6–8].

RIXS is an electronic scattering process involving the excitation of a system, in its initial (often electronic ground

state, to a core-excited intermediate state followed by decay into a final state [3]. The RIXS channel where the final state is the same as the initial state corresponds to elastic scattering, whereas inelastic scattering involves differences in electronic or nuclear degrees of freedom of the initial and final state wave functions. Hence, with sufficient energy resolution, RIXS can be used to study many kinds of excitation processes with an energy selectivity created by the intermediate core-excited state, which is targeted by tuning the energy of the incoming photons [7,9]. A final (ground or valence-excited) state, |*VE*_{*i*}, is populated if the RIXS channel to the final state is allowed from the initial (ground) state, |*VE*₀, via the intermediate (core-excited) state, |*CE*_{*i*}, i.e., if the transitions involved |*VE*₀ → |*CE*_{*i*} and |*CE*_{*i*} → |*VE*_{*i*} are both simultaneously allowed. Thus symmetry selection rules play a pivotal role in the formation of a RIXS spectrum and can be analyzed in terms of both dipole transition moments and point group symmetry. Often if |*VE*₀ → |*VE*_{*i*} is forbidden as a direct transition, the corresponding RIXS channel may be allowed in the three-level scattering process [10,11]. This opens up an avenue to observe optical dark states. However, the purely electronic symmetry selection and propensity rules can be broken in the presence of vibronic couplings as has been extensively discussed [6]. The effect of breakage and restoration of these symmetry rules are most interesting and profound in molecules having inversion symmetry, of which SF₆ is a particularly interesting example [12,13]. This breakage of symmetry can not only be brought on by vibronic

*These authors contributed equally to this work.

†odelius@fysik.su.se

Published by the American Physical Society under the terms of the [Creative Commons Attribution 4.0 International](https://creativecommons.org/licenses/by/4.0/) license. Further distribution of this work must maintain attribution to the author(s) and the published article's title, journal citation, and DOI. Funded by [Bibsam](https://www.bibsam.org/).

coupling at small distortions from the Franck-Condon region, but may even involve ultrafast bond dissociation, due to strong forces in the core-excited state in the Franck-Condon region of the ground state. If a system involving light nuclei populates an intermediate state which has a dissociative potential with a large gradient, the system undergoes an ultrafast bond cleavage dynamics on the same timescale as the relaxation to final state [14,15]. Thus the RIXS signal contains information about changes in electronic structure and chemical bonding during ultrafast dynamics in the intermediate or final states. Moreover, with high enough energy resolution, RIXS can probe the vibrational quantum levels in the final states, and thus in principle shed light on the shape of the potential energy surface along that particular degree of freedom, associated with vibrational excitations [16]. Quasielastic scattering back into the electronic ground state is a particularly powerful probe of vibrational structure, since the quasielastic vibrational progression is usually nicely separated from the electronically inelastic RIXS bands [6,15,17]. A particular effect observed in the presence of vibronic coupling or ultrafast dissociation is core-hole localization, which has been observed in simple diatomics and other symmetric molecules [18–20]. It is important to notice that the vibronic coupling of core-excited states and related core-hole localization in symmetric polyatomic molecules can have very strong influence due to intrinsic near-degeneracy of core-hole states. This motivates us to use a model based on the core-hole localization in one of the F atoms of the SF₆ molecule [6,21–23].

SF₆ has been investigated extensively using x-ray spectroscopic techniques. These include studies done at the sulfur *K* and *L* edges [24] and the fluorine *K* edge [13]. The dissociation dynamics of SF₆ following a soft ionization has also been measured using time-resolved sulfur *L*-edge x-ray absorption (XA) spectroscopy [25]. Electron vibrational coupling in SF₆ has been investigated using soft x-ray spectroscopy [26]. Additionally, vibrational wave packets in the SF₆ molecule have recently been investigated using soft-transient XA spectroscopy [27]. Recently there also have been measurements of nonresonant XE and RIXS at the fluorine *K* edge [13]. For SF₆, in its equilibrium geometry, having O_h symmetry and six equivalent F atoms, each frontier molecular orbital (MO) can be classified locally into having σ and π symmetry around the S-F bonds. Ekholm *et al.* [13] showed using nonresonant XE measurements and computation of the dissociative dynamics along the F₅S-F bond how peaks associated with S-F bonds vanish with only the σ and π features, from the dissociating ionized F atom, remaining as the S-F bond dissociates. The S-F bond dissociation following a F1s \rightarrow 6a_{1g} transition has been studied by observing Auger-Doppler effect [28] using circularly polarized x-ray.

It has also been suggested in that study that the sharp feature observed in the RIXS spectra at the lowest resonance, |F1s⁻¹6a_{1g}¹⟩, in the F1s XA spectrum can be associated with ultrafast S-F bond elongation and dissociation, similar to atomic and pseudoatomic features in HBr and H₂O [14,29].

In the present study, spectrum simulations were derived strictly from calculations of electronic states, allowing for a direct comparison of XE and RIXS features, in contrast to the previous study by Ekholm *et al.* [13] in which Kohn-Sham orbitals form the basis of analysis.

First, we simulated fluorine *K*-edge XE of SF₆, as well as RIXS at different excitation energies of the XA spectrum. These theoretical XA, XE, and RIXS spectra, performed at the ground-state optimized static geometry, are denoted as static spectrum simulations. We modeled the polarization-dependent RIXS spectra, with horizontal and vertical polarization of the incident radiation, and found that a localized core-hole picture gives a more accurate reproduction of the experimental RIXS spectra than when using the delocalized canonical orbitals, due to a breakdown of the parity selection rule. This is indicative of a strong role of vibronic coupling, ultrafast dissociation, and core-hole localization in the F1s RIXS process. In addition, we also computed the electron-hole coupling, and we found negligible couplings for the t_{1u} and t_{2g} resonances in contrast to the a_{1g} resonance.

Second, we performed wave packet dynamics to probe the dynamical aspects of the RIXS process and investigate the mechanism leading to the sharp feature in the RIXS at a_{1g} F1s XA resonance [13]. We observed that the steepness in potential energy surface of the intermediate state, i.e., the core-excited state, has a profound role in the sharpness of the RIXS spectrum.

The paper is organized as follows. Our theoretical approach is outlined in Sec. II where we describe details of simulations of F1s XA, nonresonant F1s XE, and F1s RIXS. Section III collects results of our calculations of XA, XE, and RIXS accompanied by the comparison with the experimental data. Analysis of the role of nuclear dynamics is presented in Sec. III E. Our findings are summarized in Sec. IV. Atomic units are used throughout the paper unless otherwise stated.

II. METHODS

From vertical transitions at the ground-state equilibrium geometry, static simulations of F1s XA, RIXS, and XE spectra were performed. Energies and transition moments of the electronic states were calculated with density functional theory (DFT) in the ORCA package version 4.2.0 [30], using both the restricted open shell configuration interaction singles [31] (DFT-ROCIS) and linear response time-dependent DFT (TD-DFT) protocols [32]. In addition, the transition potential method (TP-DFT) for full core-hole excitation (XFH) [33] in the CP2K program suite [34] was used for obtaining a more accurate potential energy surface for the lowest core-excited state.

Calculations of spectra were performed using states derived from core holes from either delocalized canonical F1s or localized F1s core orbitals. In addition, a one-dimensional cut in each potential energy surface was calculated for a rigid scan along a S-F bond, as a basis for wave packet dynamics simulations of the XA spectrum and RIXS against the |F1s⁻¹6a_{1g}¹⟩ resonance.

A. Quantum chemistry

The geometry of SF₆ was optimized in the Gaussian-16 program package [35] using the M06-2X hybrid functional [36], which is known to perform well in predicting structures of main group element compounds [37]. All calculations were performed with the def2-TZVP basis set [38]. The optimized geometry has O_h symmetry with a S-F bond distance of

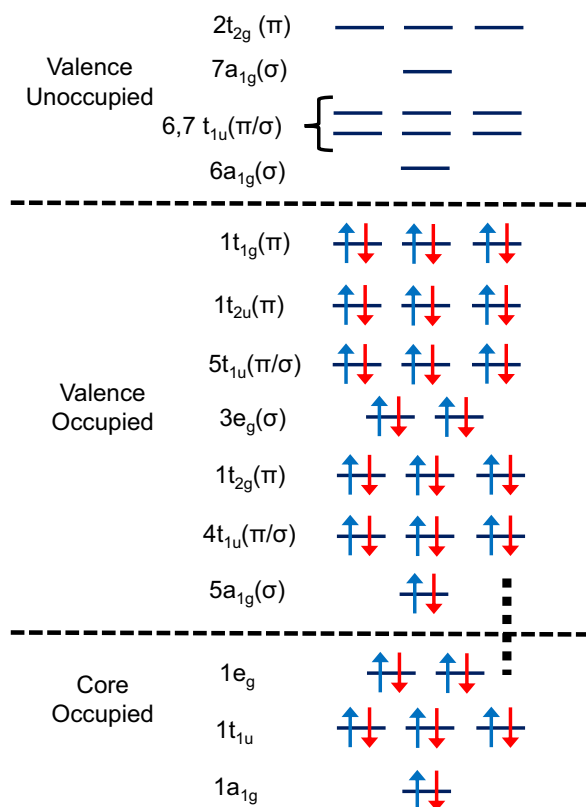


FIG. 1. Molecular orbital diagram for SF_6 in O_h symmetry, focusing on orbitals of importance for $\text{F}1s^{-1}$ RIXS and XE spectra. The dotted vertical line denotes the omission of lower valence orbitals. Refer to Figs. S1, S2, S3 for the plots of the molecular orbitals.

1.559 Å, compared to experimental values of 1.561 Å [39] and 1.564 Å [40].

The Kohn-Sham orbitals involved in the dominant XA, XE and RIXS features are classified into irreducible representations in O_h symmetry as shown in Fig. 1 and Figs. S1, S2, and S3 in the Supplemental Material [41].

1. Simulations of XA spectra

The XA spectra were computed in the ORCA package [30] at the DFT-ROCIS/B3LYP and TD-DFT levels of theory, both of which are based on utilization of an orbital selection window to consider only excitation from the core orbitals to the unoccupied orbitals. The core-hole lifetime broadening (Γ) of $\text{F}1s$ core-excited states was estimated to be 0.194 eV. [42,43]. However, spectral lines convoluted with this broadening have narrow peaks compared to experiments [44] due to neglect of vibrational broadening and experimental broadening. The discrete vertical excitations produced by DFT-ROCIS and TD-DFT were convoluted with a Voigt profile with Lorentzian full-width half-maximum (FWHM) of 0.4 eV and a Gaussian FWHM of 0.3 eV.

Additionally, TD-DFT, within the restricted subspace approximation protocol, was used to compute RIXS, which we discuss in detail later. We found the predicted core-excited state energies from TD-DFT, within the restricted subspace approximation for RIXS computation and XA only compu-

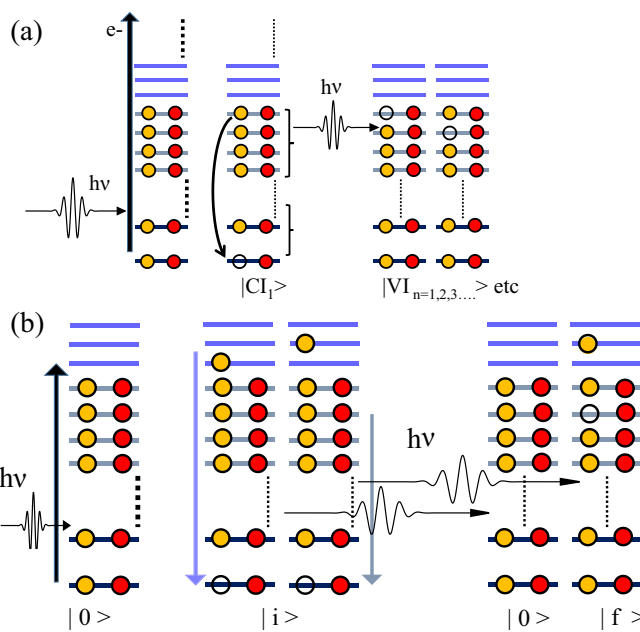


FIG. 2. Comparison between the XE and RIXS processes. The blue (dark gray), gray, and black horizontal lines denote the unoccupied, valence occupied and core occupied molecular orbitals respectively. Panels (a) and (b) show the orbital (one-electron) representation for the XE and RIXS processes, respectively.

tion, to differ by less than 0.05 eV and produce the same relative intensities.

2. Simulations of XE spectra

For XE, in contrast to RIXS, the states and transition moments need to correspond to a two-level problem, involving decay from a single core-ionized state ($|CI\rangle$) into different valence-ionized states ($|VI_i\rangle$); see Fig. 2(a). Still the process is initiated by a core-ionization of the electronic ground state. The $|CI\rangle \rightarrow |VI_i\rangle$ emission process involves the decay of an electron from the occupied molecular orbitals (valence or core), with lower binding energy, to the hole in the ionized core orbital, having higher binding energy. This is depicted pictorially in Fig. 2(a).

Here we present a protocol in which we use the RIXS module within the DFT-ROCIS level of theory as implemented in ORCA to compute the XE spectrum. Initially an ionized (doublet ground state) state of the molecule (initially with a closed shell ground state before ionization) is computed giving the energy and wave function of $|VI_1\rangle$ as shown in Fig. 3. Subsequently, primary and secondary donor spaces and acceptor space are defined to generate the core-ionized $|CI\rangle$ states and the excited valence-ionized states $|VI_{n=1,2,3,\dots}\rangle$ as depicted in Fig. 3. The RIXS module generates the transition dipole moments for the $|CI\rangle \rightarrow |VI_{n=1,2,3,\dots}\rangle$ emission processes, and the discrete spectrum is convoluted accordingly for comparison to experimental data. This protocol has been used in accurate calculations of XE spectra of C_2H_4 , C_3H_4 , and C_4H_6 [45] and discussed therein in further detail.

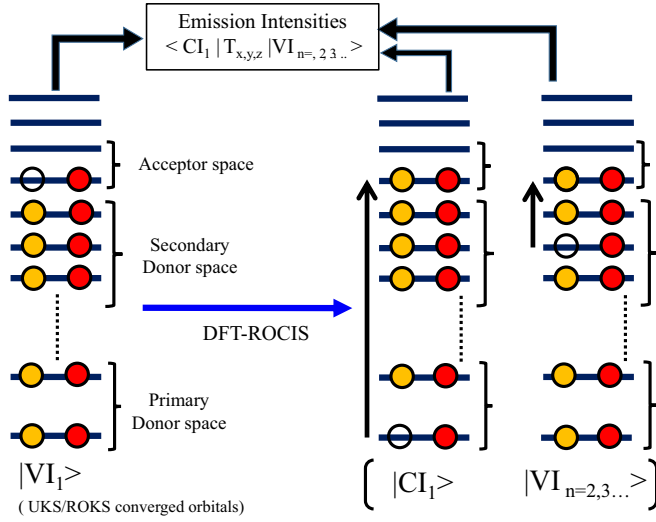


FIG. 3. Modified DFT-ROCIS protocol for computation of XE spectra. The modified DFT-ROCIS protocol first reported in Ref. [45] for computation of XE spectra is pictorially presented. The vertical black arrows indicate single excitations in the DFT-ROCIS protocol generating excited valence-ionized and core-ionized states from the reference UKS/ROKS wave function. The states obtained are used to compute transition dipole moments for the emission spectra, $\langle CI_1 | T_{x,y,z} | VI_{n=1,2,3,\dots} \rangle$, as shown at the top of the figure.

3. Simulations of RIXS spectra

Regardless of computational protocol, simulations of RIXS spectra require an accurate description of the initial (ground state) $|0\rangle$, intermediate core-excited state $|i\rangle$, and final ground or valence-excited $|f\rangle$ states [see Fig. 2(b)] and of all corresponding transition moments for all the excitations, $\mu_{(0i)}$, and emission, $\mu_{(if)}$, processes. The dipole approximation can be applied since we are dealing with soft x-rays, and the RIXS spectra are simulated according to the Kramers-Heisenberg formula [46]. *Static RIXS* spectra are calculated using the ground-state equilibrium geometry only, neglecting the evolution of the nuclear coordinates, occurring in the intermediate core-excited state or final state, in the RIXS process. However, notice here that the spectra are calculated with a localized F1s core hole, under the assumption that this process is very fast. The F1s orbitals were localized using the Foster Boys Localization [47]. In addition, we also performed simulations of *dynamical RIXS* spectra by inclusion of nuclear dynamics in one dimension, again under the assumption of instantaneous core-hole localization. Importantly, we notice that diffraction between scattering against different fluorine atoms is neglected [18–20], but the processes of core-hole localization and multicenter scattering will be considered in future studies. Also dynamics in other degrees of freedom is neglected.

As we are interested in the polarization dependence in both static and dynamical RIXS spectra, we extract the transition dipole moments between $|0\rangle$, $|i\rangle$, and $|f\rangle$, which denotes the electronic ground state, the core-excited intermediate state, and final valence-excited states, respectively, and based on these transition dipole moments $\vec{\mu}_{0i} = \langle 0 | \vec{r} | i \rangle$ and $\vec{\mu}_{if} =$

$\langle i | \vec{r} | f \rangle$, we computed the polarization-dependent RIXS,

$$\sigma(\omega', \omega) = r_0^2 \frac{\omega'}{\omega} \sum_f |F_f|^2 \Delta(\omega - \omega' - \omega_{f0}, \Gamma_f), \quad (1)$$

where ω and ω' are the incoming and outgoing photon frequencies, respectively. $\omega_{f0} = (\epsilon_f - \epsilon_0)/\hbar$ is the transition frequency difference between the initial state and the final state, r_0 is the classical electron radius, and $\Delta(\Omega, \Gamma_f) = \Gamma_f/\pi(\Omega^2 + \Gamma_f^2)$ is a Lorentzian function with the lifetime broadening [half-width at half-maximum (HWHM)] Γ_f of the final state. The scattering amplitude to any given final state is given by the Kramers-Heisenberg formula [6]

$$F_f = \sum_i \omega_{if} \omega_{i0} \frac{\langle f | \vec{e}' \cdot \vec{r} | i \rangle \langle i | \vec{e} \cdot \vec{r} | 0 \rangle}{\omega - \omega_{i0} + i\Gamma}, \quad (2)$$

where Γ_i is the core-hole lifetime broadening.

Then the total cross section reads

$$\sigma(\omega', \omega) = r_0^2 \frac{\omega'}{\omega} \sum_f \sum_{\alpha, \beta, \gamma, \delta} (e'_\alpha e'_\beta e_\gamma e_\delta) \times \sigma_{\alpha\beta\gamma\delta}^{(f)} \Delta(\omega - \omega' - \omega_{f0}, \Gamma_f), \quad (3)$$

where

$$\sigma_{\alpha\beta\gamma\delta}^{(f)} = \sum_{i,j} \omega_{if} \omega_{jf} \omega_{i0} \omega_{j0} \frac{\mu_{fi}^\alpha \mu_{jf}^\beta \mu_{i0}^\gamma \mu_{j0}^\delta}{(\omega - \omega_{i0} + i\Gamma)(\omega - \omega_{j0} - i\Gamma)}. \quad (4)$$

Here the Greek indices $\alpha, \beta, \gamma, \delta$ label the Cartesian components x, y, z of the polarization vector \vec{e} and transition dipole moment $\vec{\mu}$.

Last, we should average the RIXS cross section over molecular orientations and orientations of the final photon polarization around the momentum \vec{k}' of the scattered x-ray photon [48]

$$\overline{\sigma(\omega', \omega, \chi)} = \frac{1}{30} \sum_f \sum_{\alpha, \beta} \left[(3 + \cos^2 \chi) \sigma_{\alpha\alpha\beta\beta}^{(f)} + \frac{1}{2} (1 - 3 \cos^2 \chi) (\sigma_{\alpha\beta\alpha\beta}^{(f)} + \sigma_{\alpha\beta\beta\alpha}^{(f)}) \right]. \quad (5)$$

Here χ is the angle between the incoming photon polarization \vec{e} and the wave vector of the emitted photon \vec{k}' defined as $\cos \chi = \vec{e} \cdot \vec{k}'$.

According to our simulations the dominant contribution to the RIXS cross section is given by one-electron transitions. In this case the RIXS process is simply the core-excitation $F1s \rightarrow \psi_i$ followed by the emission transition $\psi_f \rightarrow F1s$. The final state $|\psi_f^{-1} \psi_i^1\rangle$ with the hole in MO ψ_f and electron on the unoccupied MO ψ_i allows for only one core-excited state $|F1s^{-1} \psi_i^1\rangle$. This means that the interference between electronic intermediate states is absent. However, the interference between intermediate vibrational states is very important.

This approximation allows us to get from Eq. (5) the following expression for the RIXS cross section [6]:

$$\begin{aligned} \overline{\sigma(\omega', \omega, \chi)} &= \frac{1}{9} \sum_{fi} \frac{\omega_{i0}^2 \omega_{if}^2 |\bar{\mu}_{0i}|^2 |\bar{\mu}_{if}|^2}{(\omega - \omega_{i0})^2 + \Gamma^2} \\ &\quad \times (1 + \mathcal{R}_{if}(3 \cos^2 \chi - 1)) \\ &\quad \times \Delta(\omega - \omega' - \omega_{f0}, \Gamma_f), \\ \mathcal{R}_{if} &= \frac{1}{10} (1 - 3 \cos^2 \varphi_{if}), \quad \varphi_{if} = \angle(\bar{\mu}_{0i}, \bar{\mu}_{if}), \end{aligned} \quad (6)$$

where the scattering anisotropy \mathcal{R}_{if} depends on the angle φ_{if} between the transition dipole moments of the core excitation and emission transitions.

4. DFT-ROCIS

The DFT-ROCIS protocol [31] was developed in ORCA [30] to simulate *K*- and *L*-edge XA and RIXS spectra of transition metal complexes, which are particularly challenging and require efficient algorithms. However, it has been shown to accurately predict the XA and RIXS spectra of main group element compounds [45], and thus can be for the fluorine *K*-edge spectra of SF₆. For RIXS simulations, the DFT-ROCIS method requires defining three manifolds of orbitals, which are derived from the ground-state wave function. A selected range of core orbitals, depending on the absorption edge of interested, forms the first donor space, from which single excitation generates the core-excited states. A selected range of initially doubly and singly occupied valence orbitals form the secondary donor space, and these are involved in the single excitations to generate the valence-excited states. An acceptor space is formed by selecting a suitable number of initially singly occupied and unoccupied orbitals, into which electrons from the donor spaces are excited. Here we have used the B3LYP functional and furthermore employed the RIJCOSX approximation [49] to speed up the computation.

The energy range of the RIXS spectra shown by Ekholm *et al.* [13] can be modeled by inclusion of two core electrons and 36 valence electrons in 19 (1 + 18) doubly filled orbitals and 13 unoccupied orbitals, when using a localized F1s core level. Hence, the large numbers of configuration state functions and valence-excited states make it very demanding to perform more accurate Complete Active Space Self Consistent Field (CASSCF)/Complete Active Space Perturbation Theory (CASPT2)/N-Electron Valence Perturbation Theory (NEVPT2) calculations with an (38e,32o) active space. This is perhaps a good candidate to be studied using the Density Matrix Renormalization Group (DMRG)-CASSCF/NEVPT2, but solving for a large number of states is a challenge and it was not attempted.

5. TD-DFT

RIXS was also simulated with TD-DFT in ORCA [30] within the restricted subspace approximation [50]. In TD-DFT (and DFT-ROCIS), the core-valence separation [51] is usually employed to reach core excitations without having to describe the vast amount of valence excitations between the core excitations and the ground state. This is implemented in

ORCA by restricting the orbital excitation space to just the core orbitals. In restricted subspace approximation TD-DFT, as described in Ref. [50], the core orbitals are rotated into a previously selected orbital subspace already containing a set of valence occupied and unoccupied orbitals, and excitation among all these orbitals is considered to model core-excited and valence-excited states.

The protocol involves rotation of the core orbitals into a restricted space of valence orbitals, to form a combined occupied orbital from which excitation happens into a restricted space of virtual orbitals. All excitations, realizable from the restricted spaces, are solved for to ensure the presence of both core-excited and valence-excited states, i.e., $|i\rangle$ and $|f\rangle$, respectively.

The TD-DFT protocol has the advantage of being more flexible than the DFT-ROCIS protocol in terms of choice of functional approximations, since DFT-ROCIS is parameterized for B3LYP and BHANDHLYP only, whereas TD-DFT can be used with any functional. For direct evaluation against DFT-ROCIS, we performed TD-DFT calculations using both the B3LYP functional and the CAM-B3LYP functional [52] in the present study, keeping in mind that CAM-B3LYP is a range-separated functional which can accurately account for valence-excited states and can more accurately reproduce excited state potential energy surfaces, which will be later used to take into account dissociative dynamics. The RIJCOSX approximation was used for all TD-DFT calculations [53], along with Tamm-Dancoff approximation [54].

For the TD-DFT simulation of RIXS at the $|F1s^{-1}6a_{1g}^1\rangle$, $|F1s^{-1}6/7t_{1u}^1\rangle$, and $|F1s^{-1}2t_{2g}^1\rangle$ resonances, 17 doubly occupied valence orbitals, with the omission of the $5a_{1g}$ orbital from the set of orbitals considered in Ekholm *et al.* [13], were taken as the orbital space to generate the valence excitation. One localized core F1s orbital was rotated into the selected orbital space, thus forming the combined doubly occupied donor space. The 11 lowest lying virtual orbitals were taken into the orbital subspace. Hence, the subspace TD-DFT calculation included (1 + 17) occupied orbitals and 11 unoccupied orbitals. It is worth mentioning here that in the DFT-ROCIS protocol all the orbitals described above were included, along with the additional $5a_{1g}$ orbital, i.e., (1 + 18) occupied orbitals and 13 unoccupied orbitals.

6. XFH TP-DFT

An alternative description of the potential of the lowest core-excited state was obtained with the XFH TP-DFT protocol in the CP2K program suite [34]. Calculations of SF₆ were performed in a cubic cell with side 20 Å and a Poisson solver for isolated systems [55] using a 600 Ry kinetic energy cutoff for the plane wave part of the description of the electron density in the Gaussian augmented plane wave (GAPW) method. These were all-electron calculations employing the B3LYP functional and def2-TZVP basis sets [38]. Broken symmetry was used to facilitate the description of a ground state with unrestricted wave function in the dissociation limit. Subsequent to the SCF of the ground-state wave function, all seven 1s orbitals were involved in the localization to obtain a F1s orbital on the fluorine atom, which was core excited in the XFH TP-DFT protocol [33].

B. Wave packet nuclear dynamics for accessing effect of S-F bond dissociation dynamics on the RIXS spectrum

Ekhholm *et al.* [13], demonstrated that SF₆ upon ionization follows a single S-F bond dissociation, preserving five other S-F bonds, which with a particular S-F bond distance reaching 2 Å in the 10 fs timescale. The XE spectrum was found to be significantly dependent on the bond dissociation dynamics, as suggested by simulations reported in Ekhholm *et al.* [13]. We have additionally carried out an *ab initio* molecular dynamics on the |F1s⁻¹6a_{1g}¹⟩ core-excited state surface, using the MD module implemented in the ORCA package. The dynamics was simulated employing core-excited state from localized F1s orbitals and with a time step of 0.1 fs. The neglect of nonadiabatic effects is motivated by restrictions to a single localized core hole and excitation into the resonance, which is energetically well separated from the other resonances. The dynamics on the core-excited state followed a very much similar trend of that of the core-ionized state. The dynamics is dominated by an ultrafast single S-F bond dissociation; see Fig. S4. The changes in the other five S-F bond distances are smaller in magnitude. Pyramidalization and angular distortions were also observed but were small in magnitude and would be significant only at timescales much longer than the core-hole lifetime. Thus a minimalistic, yet accurate, model to access the effect of excited state dynamics on the RIXS spectrum, especially at the |F1s⁻¹6a_{1g}¹⟩ resonance, could be achieved by constructing rigid scans along dissociation of a single S-F bond keeping all other modes fixed.

1. Potential energy surfaces

Realistic simulations of wave packet dynamics rely upon accurate potential energy surfaces (PES), and for cases of S-F bond dissociation in the RIXS or XE process, an extended region leading to the formation of F· and SF₅· radicals has to be described. For simulations of F1s RIXS, we have used TD-DFT/CAM-B3LYP and DFT-ROCIS/B3LYP computations as implemented in ORCA to compute a one-dimensional cut in the PES of relevant electronic states along a rigid scan of dissociation of a single S-F bond; see Figs. S5–S14 for DFT-ROCIS PES and Figs. S15–S21 for TD-DFT PES. The dissociation limit is not possible to account for in DFT, and TD-DFT used here accounts for only one-electron excitations (CIS). Hence, we follow the scan only to the point where the ground-state wave function is predominantly single reference, i.e., a S-F distance of 1.31 Å to 2.16 Å as cross-checked by a CASSCF(2,2) computation. This protocol yields the energies and the wave functions for ground, valence-excited, and core-excited states, i.e., |0⟩, |f⟩, and |i⟩. The RIXS module is used to obtain the transition dipole moments, $\vec{\mu}_{0i}(R)$ and $\vec{\mu}_{if}(R)$ for each |0⟩ → |i⟩ and |i⟩ → |f⟩ transition along the scan.

The states from the quantum chemical calculations are in the adiabatic representation and undergo crossings and avoided crossing along the scan. By following the character of the states and ensuring continuous evolution of transition dipole moments to the core excited and electronic ground state, we very crudely obtain PES of states in an approximately diabatic representation. The couplings between these states are neglected in the simulations. On the basis of the uncoupled diabatic states, wave packet simulations can be

performed for the F 1s XA spectrum and corresponding RIXS spectra at different resonances.

2. Wave packet model

To describe the fragmentation of SF₆ in the core-excited state, we constructed a one-dimensional wave packet model along the S-F bond R . Assuming the (F)₅S moiety is rigid and fixed, the reduced mass will be given simply by the mass of the fluorine atom $\mu \approx m_F = 18.998$ amu. The core-hole lifetime at the fluorine K edge is $2\Gamma = 0.194$ eV where Γ is the HWHM [43]. Hence the nuclear Hamiltonian of the system on the i th electronic state will be $H_i = p_R^2/2\mu + V_i(R)$, where $R \equiv r_{S-F}$, and $V_i(R)$ is the potential energy curve of the i th state. Upon dissociation, the wave packet can access highly stretched bond configurations, meaning we have to take into account the dependence of the electronic transition dipole moments on the R coordinate. For the case of a 1D model, the transition dipole moments do not change orientation during the dynamics, hence we can write $\vec{\mu}_{fi}(R) = \hat{\mu}_{fi}(R_0) \times \mu_{if}(R)$, where $\hat{\mu}_{fi}(R_0)$ is the unitary transition dipole moment at the GS equilibrium distance R_0 and $\mu_{if}(R)$ is the modulus of the transition dipole moment as a function of R . Hence, we can rewrite the RIXS cross section beyond the Franck-Condon approximation by generalizing Eq. (4):

$$\sigma_{\alpha\beta\gamma\delta}^{(f)} = \sum_i \omega_{if}^2 \omega_{i0}^2 \hat{\mu}_{fi}^\alpha \hat{\mu}_{if}^\beta \hat{\mu}_{i0}^\gamma \hat{\mu}_{0i}^\delta \times \sigma_{\text{vib}}(\omega', \omega), \quad (7)$$

$$\sigma_{\text{vib}}(\omega', \omega) = \frac{1}{\pi} \text{Re} \int_0^\infty dt \langle \Psi(0) | e^{-iH_f t} | \Psi(0) \rangle e^{i(\omega - \omega' - \omega_{f0} + \epsilon_{v_0} + t\Gamma)t}, \quad (8)$$

$$|\Psi(0)\rangle = \mu_{if}(R) \int_0^\infty dt e^{-iH_i t} \mu_{i0}(R) |v_0\rangle e^{i(\omega - \omega_{i0} + \epsilon_{v_0} + t\Gamma)t}, \quad (9)$$

where $\hat{\mu}_{fi}^\alpha = \mu_{fi}^\alpha / \mu_{if}$ and $|\Psi(0)\rangle$ is the time-integrated wave packet, which contains the dependence on the nuclear motion as well as excitation energy in the RIXS process [56]

III. RESULTS

The simulation of the various x-ray spectroscopic signatures for SF₆ at the fluorine K edge is presented herein. We start with the theoretical analysis of static XA spectra, and proceed with a detailed scrutiny of RIXS and XE spectra. It should be noted here that dynamical effects in the XA process are discussed in the context of wave packet simulations of RIXS.

We notice that computations give identical XA spectra, regardless of performed whether in the frame of canonical (delocalized) core holes or in the frame of localized core holes. Similarly, for the XE spectrum the localization does not matter, since decay from all six core holes are considered in both frames. In contrast, for the RIXS process the symmetry selection rules change, from using delocalized core holes (O_h symmetry of the molecule) to using localized core hole.

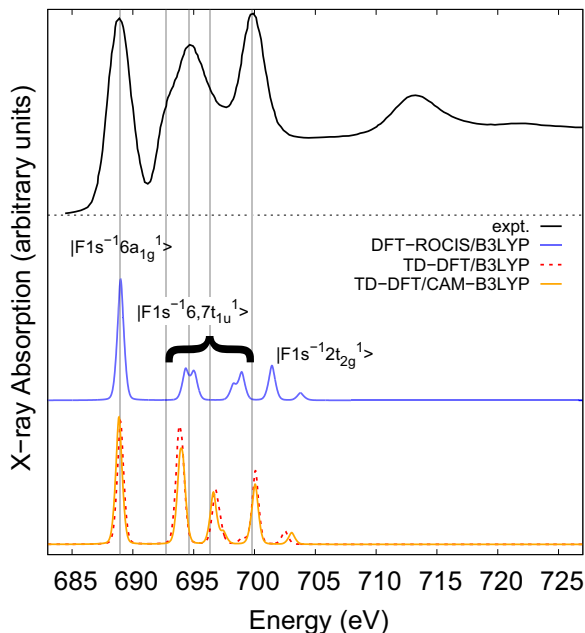


FIG. 4. Fluorine *K*-edge x-ray absorption spectrum of SF₆. Static F1s XA spectra obtained within the frameworks of DFT-ROCIS [blue (dark gray) line], TD-DFT/B3LYP [red-dotted (dark gray) line], and TD-DFT/CAM-B3LYP [orange (light gray) line]. The experimental spectrum is reproduced from Ref. [24]. The symmetry of the corresponding unoccupied orbital that the F1s electron gets excited into is labeled along with the peaks. The computed spectra are normalized to the $|F1s^{-1}6a_{1g}^1\rangle$ peak.

A. The fluorine *K*-edge XA spectrum

The fluorine *K*-edge XA spectrum for SF₆ was computed at different levels of theory. For the static XA spectrum calculations in Fig. 4, the core excitations were considered using both localized and delocalized core holes, yielding the same spectra.

Computed static XA spectra are presented in Fig. 4 alongside the experimental spectrum from Hudson *et al.* [24]. The computed spectra were blueshifted by 20.1, 18.7, and 18.1 eV for DFT-ROCIS/B3LYP, TD-DFT/B3LYP, and TD-DFT/CAM-B3LYP, respectively, to align to the $|F1s^{-1}6a_{1g}^1\rangle$ peak of the experimental spectrum. We notice that these constant shifts of the computed XA spectra align with all other pre-edge peaks with the experimental data within ± 2 eV.

We see that the different levels of theory consistently predict a weaker intensity peak for the $|F1s^{-1}2t_{2g}^1\rangle$ resonance, than experimentally observed. However, in the experiment the $|F1s^{-1}2t_{2g}^1\rangle$ peak could have increased intensity from the higher transitions that we don't capture at TD-DFT or DFT-ROCIS. Also dynamical effects due to the dissociative nature of core-excited states would alter the intensity ratios, along with photoionization effects. Using TD-DFT both CAM-B3LYP and B3LYP predict almost a similar spectra. DFT-ROCIS, however, predicts splittings in the $|F1s^{-1}6, 7t_{1u}^1\rangle$ states and much lower intensities as compared to the $|F1s^{-1}6a_{1g}^1\rangle$ peak.

The 6, $7t_{1u}$ unoccupied orbitals, having the same symmetry, are involved in core-excited states that can couple and

give splitting of the peaks, which has been discussed earlier by Hudson and coworkers [24] as three peaks, arising from transitions to these t_{1u} orbitals, while fitting their experimentally observed XA spectrum. It has been also described in Ref. [24] that between the $|F1s^{-1}6t_{1u}^1\rangle/|F1s^{-1}7t_{1u}^1\rangle$ and the $|F1s^{-1}2t_{2g}^1\rangle$ peaks, there exists a very low-intensity peak arising due to the transition to the $7a_{1g}$ orbital; see experimental spectra in Fig. 1. However, we consistently fail to get a peak due to transition to the $7a_{1g}$.

The DFT-ROCIS and TD-DFT computations consistently failed to produce the e_g peak around 713 eV, which we neglect for the present work. However, computations by Ruud and coworkers were able to simulate the sulfur $L_{2,3}$ XA spectra corresponding to this edge using real-time propagation of the Dirac-Kohn-Sham density matrix [57].

B. The fluorine *K*-edge XE spectrum

The fluorine *K*-edge XE spectrum of SF₆ has been measured by Ekholm and coworkers [13], where SF₆ was photoexcited at 751.4 eV. This photon energy is selected to be above any distinct resonances in the XA spectrum in order to probe a nonresonant decay process. Essentially, the XE process involves decay of the core ionized state $|CI\rangle$ into valence ionized states $|VI_{n=1,2,3,\dots}\rangle$, and hence provides the spectroscopic signatures corresponding to the valence orbitals, which are occupied in $|VI_1\rangle$. There are six F1s core-ionized states, also when localized, but because the fluorine sites are chemically equivalent, it is at our level of approximation sufficient to consider only one localized $|CI\rangle$. Consequently, similar to absorption, the molecular symmetry of the decaying orbitals does not come into play. Due to dipole selection rules, the XE spectrum is a result of emission originating in the decay of electrons from valence occupied orbitals, primarily having F2p character, to the ionized F1s core hole.

In this work we simulated a static XE spectrum of SF₆ with a protocol based on DFT-ROCIS RIXS module in ORCA, previously applied to a series of alkenes [45]. The details of this protocol have already been discussed in detail in the Methods Sec. II and in Ingle *et al.* [45]. In comparison to the Kohn-Sham orbital approximation presented in Fig. 3 ($\tau = 0.0fs$ spectrum) in Ekholm *et al.* [13], the present protocol results in a static XE spectrum in better agreement with the experimental spectrum in terms of the peak intensities and transition energies. Even though in this work we neglect the dynamical effects that were earlier demonstrated to be important [13], the spectrum simulated with the above mentioned protocol provides a fairly accurate estimation of the experimental XE spectrum.

The computed XE spectrum was blueshifted by 17.1 eV to achieve the best global match between the computed spectra and the experimental spectrum. The shift for the XE spectrum is different from the shift used for XA spectra, primarily because the XA spectrum was computed for a neutral species and the XE spectrum derived from the open shell ionized species. The experimental peaks above 680 eV arise from shake up states [58,59] and are absent in our simulation. As depicted in Fig. S22, the DFT-ROCIS simulated spectrum actually matches well in the emission energies corresponding to decay from the $|1t_{1g}^{-1}\rangle$, $|1t_{2u}^{-1}\rangle$, $|5t_{1u}^{-1}\rangle$, $|3e_g^{-1}\rangle$, and $|1t_{2g}^{-1}\rangle$ states,

but the intensities are not exactly reproduced. We speculate that this is due to the neglect of dynamical effects of the F₅S-F bond dissociation, which was previously shown [13], and causes the $|4t_{1u}^{-1}\rangle$, $|1t_{2g}^{-1}\rangle$, and $|3e_g^{-1}\rangle$ peaks to decrease in intensity and move to lower emission energy, whereas the $|1t_{2g}^{-1}\rangle$ peak merges with the main peak.

C. RIXS spectra at different F1s resonances

Having initially examined the XA spectrum presented in Fig. 4, we simulated the static F1s RIXS spectra of SF₆ in the same theoretical framework using DFT-ROCIS and TD-DFT. The TD-DFT protocol within the restricted subspace approximation [50] and DFT-ROCIS/B3LYP were chosen as methods of choice since they have been shown to perform well in simulating RIXS spectra in a number of earlier studies [45,60]. The computational details are given in the Methods Sec. II. RIXS spectra were calculated for each of the $|F1s^{-1}6a_{1g}^1\rangle$, $|F1s^{-1}t_{1u}(A)^1\rangle$, $|F1s^{-1}t_{1u}(B)^1\rangle$, and $|F1s^{-1}2t_{2g}^1\rangle$ resonances. Limitations in DFT-ROCIS lead to under- and overestimation of energies for the valence excitations, and hence different shifts for the XA and RIXS spectra were employed. By applying the same constant energy blueshift of 17.1 eV as for the XE spectra in Fig. S22, we allow for a direct comparison of the XE and RIXS spectra on the emission energy scale, at the expense of misaligning the elastic peak. However, this shift used in RIXS spectra, which is consistent with that used for aligning the XE spectrum, enabled us to discuss and compare both resonant and nonresonant emission spectra at a consistent and comparable level of theory, and in turn spectator-shift or binding energies could be deduced.

However, using TD-DFT the valence excited state energies are reproduced more accurately, we shift the simulated RIXS spectra to match the experimentally obtained elastic line, for individual resonances. The six F1s core orbitals forms Symmetry Adapted Linear Combination of a_{1g} , t_{1u} , and e_g symmetry; see Fig. 1 and Fig. S1. These canonical Kohn-Sham core orbitals are delocalized over all the six F atoms, which are arranged in O_h symmetry around the central S atom; see Fig. S1. Ekholm *et al.* [13] reported on the presence of core-hole localization effects and the violation of the parity selection rule in the RIXS spectra, which was concluded from the observation of peaks associated with electronically dipole forbidden transitions resulting from breaking of the global inversion symmetry.

Whereas the XA and nonresonant XE are insensitive to the choice of delocalized or localized core orbitals when considering simultaneous excitations from all six F1s core orbitals, the parity selection rule and effect of core-hole localization are decisive in RIXS [48]. In the frame of delocalized core orbitals, the $|1t_{1u}^{-1}6a_{1g}^1\rangle$ state has a parity-allowed transition from the ground state and is the sole contributor to the $|F1s^{-1}6a_{1g}^1\rangle$ resonance in the XA spectrum, since neither the $2a_{1g}^{-1}6a_{1g}^1\rangle$ nor the $|1e_g^{-1}6a_{1g}^1\rangle$ can be reached within the dipole approximation.

Comparisons of RIXS simulations (using delocalized and localized core orbitals) at the $|F1s^{-1}6a_{1g}^1\rangle$ resonance are presented in Fig. 5 in comparison to experiment. For RIXS calculations with delocalized core orbitals, the parity selection

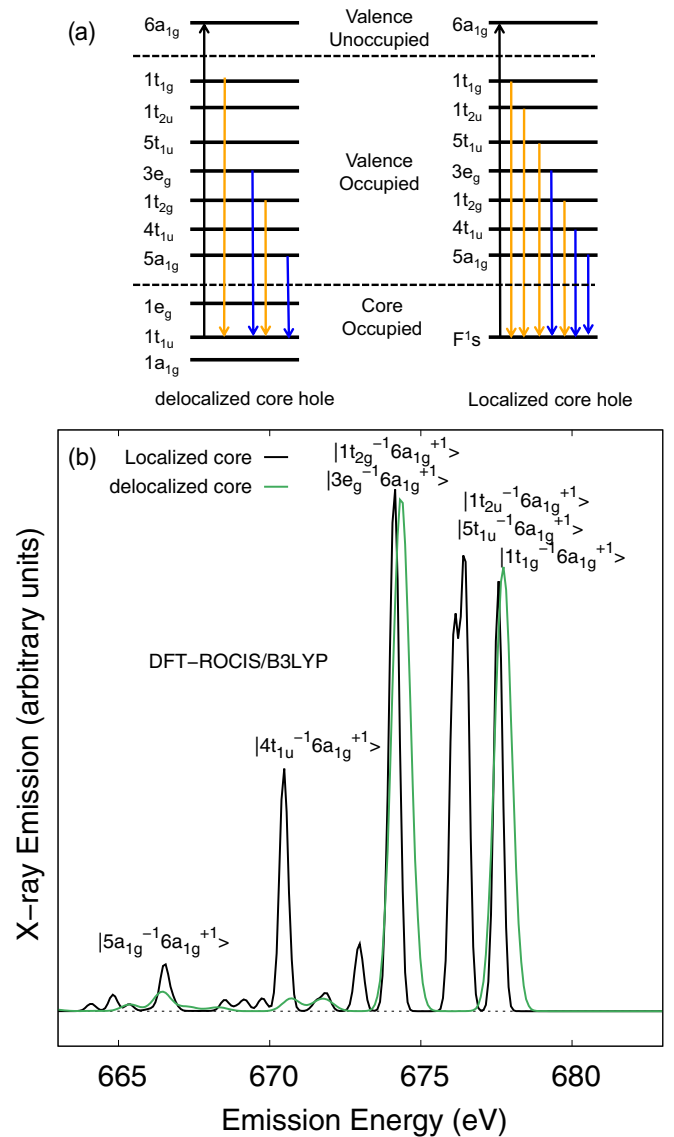


FIG. 5. Simulations of RIXS at the $|F1s^{-1}6a_{1g}^1\rangle$ resonance with delocalized and localized core-holes. (a) The symmetry of the involved orbitals is shown, and the allowed transitions are denoted by the vertical arrows. (b) The total RIXS at the $|F1s^{-1}6a_{1g}^1\rangle$ resonance computed with localized (black spectrum) and delocalized core holes [green (gray) spectrum]. The RIXS spectra simulated here are computed without considering polarization dependence or scattering anisotropy, and shown to depict the defect of delocalization and localization on the number of peaks in the RIXS spectra. Clearly the number of peaks appearing with localized core hole is larger than when using delocalized core holes, which preserves selection rules, due to breakdown of symmetry selection rules.

rule allows only for decay to the delocalized core orbital $1t_{1u}$ from valence-occupied orbitals having gerade(g) symmetry. The sharp peak in the $|F1s^{-1}6a_{1g}^1\rangle$ resonance around 677.8 eV, at which is due to transitions from the $5t_{1u}$ and $1t_{2u}$ orbital, would be absent; see Fig. 5(b), blue spectrum vs orange spectrum. However, this peak is present and also the sharpest peak in the RIXS spectra. The peaks which arise under conservation of parity selection rules among the relevant orbitals in SF₆ are shown in Fig. 5(a) along with the corresponding static RIXS

spectrum in Fig. 5(b) depicted as the blue spectrum. In contrast in the frame of localized core orbitals, the parity selection rule is broken, and the simulated RIXS spectrum, as shown by orange spectrum in Fig. 5(b), accounts for all the peaks which are experimentally observed. It should be noted that, even for RIXS, the localized and delocalized pictures are equivalent, if one includes all near-degenerate channels and interference between them. However, since vibronic coupling in the intermediate state often quenches electronic interference [61], the use of a localized picture neglecting electronic interference constitutes a pragmatic approximation which reproduces experimental observables. Based on this we proceeded to compute the RIXS spectra with a localized core-hole neglecting interference between different core-hole sites, which typically arises due to vibronic coupling. We clearly see in Fig. 5(b) that the spectrum obtained using localized core hole clearly shows all possible transitions and all the peaks in the experimental spectra can be accounted for.

Thus we proceeded to compute static RIXS spectra using DFT-ROCIS and TD-DFT for different resonances with a localized core hole and also consider the polarization dependence, which was neglected in Fig. 5, when presenting the role of localization and parity violation.

1. RIXS at the $|F1s^{-1}6a_{1g}^1\rangle$ resonance

The polarization-dependent RIXS was computed for the $|F1s^{-1}6a_{1g}^1\rangle$ resonance. In the localized description, the polarization dependence can be understood in terms of local π/σ character, and the notion that a dipole transition creates or annihilates a nodal plane perpendicular to the polarization direction. In the two-step approximation, this implies a symmetry selectivity in the absorption that leads to an angular anisotropy in the emission. The S-F bond, where the F corresponds to the localized core hole, is selected as the molecular axis. This definition is required to define the angle between the incident and emitted radiation; see Eq. (1) in Sec. II. The RIXS intensity depends on two factors: (1) if the involved occupied valence MO locally has π or σ symmetry with respect to the S-F bond and (2) the orbital amplitude of the F, on which the core hole is localized in the involved MO. The polarization-dependent RIXS intensity is an indicator of the shape and symmetry of the occupied MOs. More precisely the polarization dependence is defined by the scattering anisotropy $(\mathcal{R})_{if}$, in Eq. (6), which depends on the angle φ_{if} between the transition dipole moments of core excitation and emission transition. According to Eq. (6) the polarization dependence of the RIXS intensities is characterized by the function

$$I(\chi) = 1 + \mathcal{R}_{if}(3 \cos^2 \chi - 1). \quad (10)$$

For comparison to the experimental setup, we computed this function for two angles $\chi = 0^\circ$ and $\chi = 90^\circ$ (“horizontal” and “vertical” orientations of \mathbf{e} and \mathbf{k}'). Results of simulations for the RIXS channel at the $|F1s^{-1}6a_{1g}^1\rangle$ resonance are collected in Table I, which describe the situation shown in Fig. 6.

Thus, the polarization-dependent RIXS intensity is an indicator of the shape and symmetry of the occupied MOs. For SF₆ in O_h geometry, the occupied MOs of different character can have either local π or σ symmetry with respect to the S-F

TABLE I. Polarization of RIXS, at the $|F1s^{-1}6a_{1g}^1\rangle$ resonance, for emission transitions $\psi_f \rightarrow F1s$ from different MOs ψ_f (see Fig. 7) at the TD-DFT level of theory. Scattering anisotropy is defined as $\mathcal{R}_{if} = (1 - 3 \cos^2 \varphi_{if})/10$. We mention the ratio between polarization dependence of the RIXS intensities at two angles $\chi = 0^\circ$ and $\chi = 90^\circ$ (“horizontal” and “vertical” polarization), and $I_{\text{vert}}/I_{\text{hor}}$, with $I_{\text{vert}} = I(90^\circ) = 1 - \mathcal{R}_{if}$ and $I_{\text{hor}} = I(0^\circ) = 1 + 2\mathcal{R}_{if}$, where $I(\chi) = 1 + \mathcal{R}_{if}(3 \cos^2 \chi - 1)$, $\cos \varphi_{if} = (\vec{\mu}_{0i} \cdot \vec{\mu}_{if})/\mu_{0i}\mu_{if}$.

MO ψ_f	$\cos \varphi_{if}$	\mathcal{R}_{if}	$I_{\text{vert}}/I_{\text{hor}}$
$1t_{1g}$	≈ 0	0.1	0.9/1.2
	≈ 0	0.1	0.9/1.2
	≈ 0	0.1	0.9/1.2
$1t_{2u}$	≈ 0	0.1	0.9/1.2
	≈ 0	0.1	0.9/1.2
	≈ 0.5	0.026	0.975/1.051
$5t_{1u}$	≈ 0.7	-0.046	0.954/1.092
	≈ 0	0.1	0.9/1.2
	≈ 0	0.1	0.9/1.2
$1t_{2g}$	≈ 0	0.1	0.9/1.2
	≈ 0	0.1	0.9/1.2
$3e_g$	≈ -1	-0.2	1.2/0.6
	≈ 1	-0.2	1.2/0.6
	≈ 0	0.1	0.9/1.2
$4t_{1u}$	≈ 0.87	-0.12	1.12/0.76
	≈ -0.97	-0.18	1.2/0.64
$5a_{1g}$	≈ -1	-0.2	1.2/0.6

bond. As seen from Fig. 5(a), some of the transitions have intensities along vertical polarization whereas others have intensity along the horizontal polarization. Based on symmetry arguments, t_{1g} , t_{2g} , and t_{2u} MOs have π symmetry and hence have higher intensity along horizontal polarization, whereas e_g and a_{1g} MOs having σ symmetry have higher intensity along vertical polarization; see Table I. However, t_{1u} MOs are not uniquely defined in terms of σ and π symmetry and hence can give intensity of both horizontal or vertical polarization. In this particular case, the polarization dependence is related to the coefficient of the local F atomic orbital’s contribution to the t_{1u} MOs. We see from the MO displayed in Fig. S2 that indeed $4t_{1u}$ and $5t_{1u}$ have different polarization due to the orbital hybridization; see Table I.

In Fig. 6 we present the polarization dependence in the static RIXS spectrum for the $|F1s^{-1}6a_{1g}^1\rangle$ resonance in comparison the experimental spectrum as reported by Ekholm *et al.* [13]. We see that the simulated spectra reproduced the polarization dependence of different peaks very accurately. The isotropic orientation of the molecule has been taken care of in the computation of the polarization dependence of the RIXS signal using Eq. (5), and thus all peaks have intensity for both horizontal and vertical polarization, and the predominance of any polarization is dictated by the orientation of the S-F bond with the polarization of the incident radiation. Thus though Fig. 5(a) shows exclusively the presence of either vertical or horizontal polarization for a particular emission, the real spectra contain intensity for both polarizations for all the emissions. The emission energies of the peaks appear to be shifted to lower emission energies by almost a constant

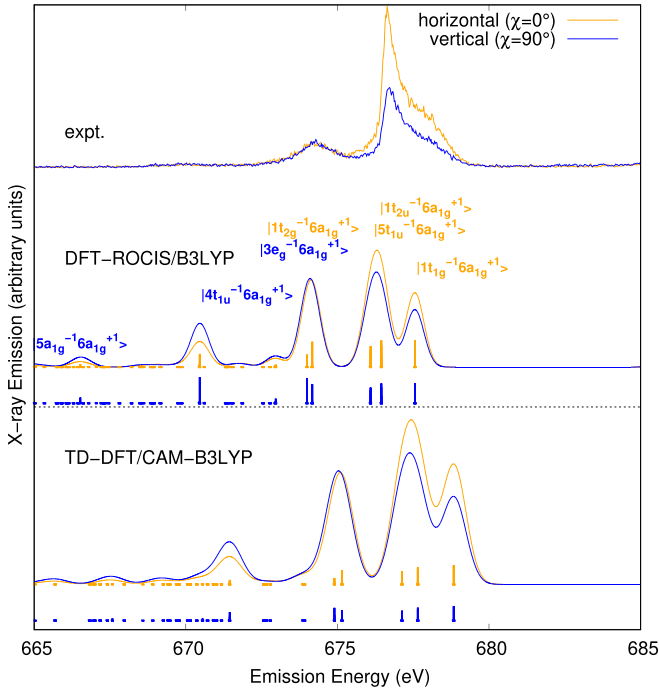


FIG. 6. Comparison between simulated polarization-dependent RIXS spectra at the DFT-ROCIS/B3LYP and the restricted subspace TD-DFT/CAM-B3LYP levels of theory for the $|F1s^{-1}6a_{1g}^i\rangle$ resonance and with experimental spectrum obtained from Ref. [13]. Both the TD-DFT and DFT-ROCIS computation were done with a localized F1s core hole, and interference between different intermediate states is neglected. The [blue (dark gray)] sticks of intensities for vertical polarization are given a downward shift for clarity and comparison with the orange (light gray) sticks representing the horizontal polarization. The polarization dependence was computed using Eq. (10) in one-electron picture. The orange (light gray) spectra indicate spectra at horizontal polarization ($\chi = 0^\circ$) and blue (dark gray) spectra represent vertical polarization ($\chi = 90^\circ$).

0.75 eV with respect to the experimental spectrum, when we use the shift used in the XE spectrum. This is due to error in estimation of the valence excited state energies by DFT-ROCIS.

Though the polarization dependence of the different peaks are accurately predicted by DFT-ROCIS, the relative emission intensities from different orbitals are not accurately reproduced. This clearly results in a much higher peak associated with $|3e_g^{-1}6a_{1g}^i\rangle$, $|1t_{2g}^{-1}6a_{1g}^i\rangle$ states and lacks the sharpness and height of the peaks associated with $|1t_{2u}^{-1}6a_{1g}^i\rangle$, $|5t_{1u}^{-1}6a_{1g}^i\rangle$ states. This effect is not only due to the shortcoming of the quantum chemical method, i.e., DFT-ROCIS, used, but also due to absence of dynamical effects in these simulated spectra. Later we have included and studied the dynamical effects on the RIXS spectra which are discussed below.

The RIXS at the $|F1s^{-1}6a_{1g}^i\rangle$ resonance was also computed at the restricted subspace TD-DFT [50] method, as discussed earlier in Methods Sec. II, since TD-DFT calculations with the B3LYP and CAM-B3LYP functionals have been known to predict valence-excited states accurately. In Fig. 6 we plot the static RIXS spectra at the $|F1s^{-1}6a_{1g}^i\rangle$ resonance, computed at the restricted subspace TD-DFT/CAM-B3LYP and

DFT-ROCIS levels of theory. The DFT-ROCIS and TD-DFT methods produce similar static RIXS spectra. However, both levels of theory consistently predict a too high peak corresponding to $|3e_g^{-1}6a_{1g}^i\rangle$ and $|1t_{2g}^{-1}6a_{1g}^i\rangle$ states, and the relative sharpness of the main peak is not captured. Thus it is shown here that though some of the essential features and position of the peaks are dependent on the method used, the entire RIXS spectra is not well reproduced using static geometry of computation, thus neglecting vibronic coupling. Essentially both the DFT-ROCIS and restricted subspace TD-DFT/CAM-B3LYP methods predict similar spectra with the same success and shortcomings common to both DFT-ROCIS and TD-DFT. However, obviously the predicted energies of the valence-excited state reflected in the RIXS spectra and energy-loss vary from one theory to the other.

2. RIXS at the $|F1s^{-1}t_{1u}^i\rangle$ resonances at three different incident energies

Ekholm *et al.* [13] report measurements of F1s RIXS at 694.6 eV. As clearly seen from the simulated spectra in Fig. 4, and suggested by Ekholm and coworkers also, this excitation involves both the $|F1s^{-1}t_{1u}^i(\pi)\rangle$ and $|F1s^{-1}t_{1u}^i(\sigma)\rangle$ core-excited states. We simulated RIXS from both these resonances separately which correspond to three discrete core-excited states distinctly separated in energy for DFT-ROCIS computation (see Fig. 4) and the RIXS spectra are plotted in Fig. 7. The RIXS experiment was also done at two more excitation energies, i.e., at 692.7 eV and 696.3 eV, which target the $6t_{1u}$ and $7t_{1u}$, respectively. We denote these two simulated resonances in Fig. 7 as DFT-ROCIS($6t_{1u}$) for $6t_{1u}$ and DFT-ROCIS($7t_{1u}$) for $7t_{1u}$.

We clearly see in the RIXS spectrum corresponding to excitation at 692.7 eV, which targets $|F1s^{-1}6t_{1u}^i\rangle$ resonance, that there is more prominent polarization dependence in the peak, around 677.8 eV, corresponding to $5t_{1u}$ and $1t_{2u}$, and for the peak around 678.5 eV corresponding to $1t_{1g}$ orbital. This is absent for the RIXS spectra excited at the 694.6 eV and 692.3 eV. Our simulated spectra corresponding to the $6t_{1u}$ clearly reproduces this strong energy dependence in the polarization consistently. We also see that the absence of prominent polarization dependence of the main peak in the RIXS at 696.3 eV excitation is also reproduced by the simulation for the $|F1s^{-1}7t_{1u}^i\rangle$ resonance.

The two resonances, $6t_{1u}$ and $7t_{1u}$, differ in σ and π symmetry depending on the definition of the molecular axis, and also the orbital amplitude of the particular F atom on which core-excitation happens. The polarization dependence for the emission involving orbitals having gerade symmetry is of particular interest: emission involving these orbitals, i.e., $5a_{1g}$ and $3e_g$ orbitals, reverse polarization dependence for the two different $|F1s^{-1}6t_{1u}^i\rangle$ and $|F1s^{-1}7t_{1u}^i\rangle$ resonances, denoted by DFT-ROCIS/B3LYP(A) and DFT-ROCIS/B3LYP(B) in Fig. 7. For the peak corresponding to the $4t_{1u}$ orbitals we also see that the polarization change is due to fact that $4t_{1u}$ has the same or different local symmetry as compared to $6t_{1u}$ and $7t_{1u}$ orbitals, respectively.

However, we also see from the experimental spectra for excitation at 694.6 eV, which is believed to excite to both $6t_{1u}$ and $7t_{1u}$ orbitals, the polarization dependence is not as

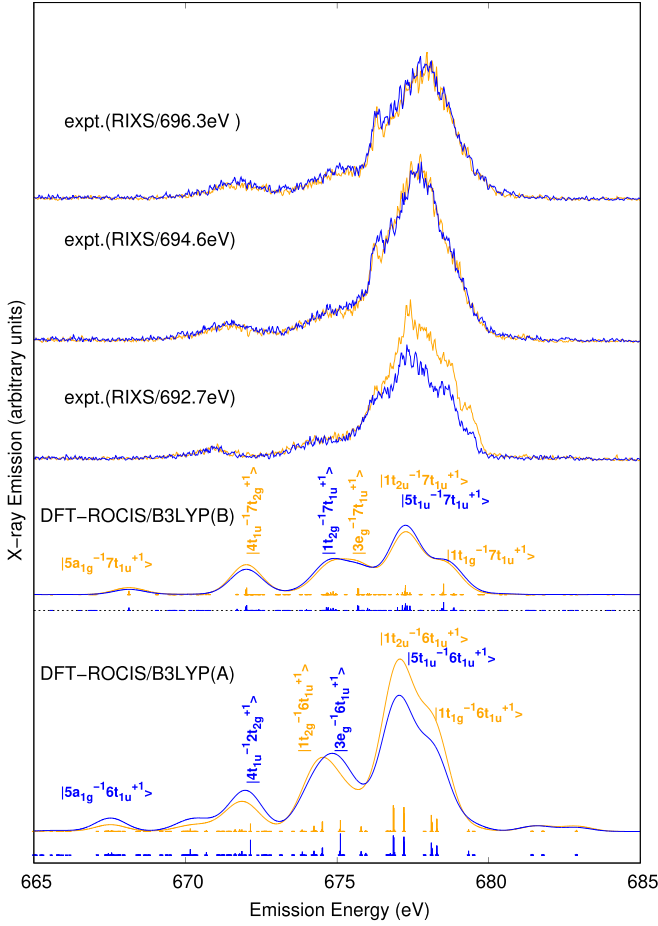


FIG. 7. Simulated polarization-dependent RIXS spectra at DFT-ROCIS level of theory for the $|F1s^{-1}7t_{1u}^1\rangle$ resonance considering a localized core hole along with experimental spectrum obtained from Ref. [13]. Three separate incidence wavelengths were used in the experiment. Here we show the spectra computed at the $|F1s^{-1}6t_{1u}^1\rangle$ and $|F1s^{-1}7t_{1u}^1\rangle$ resonance. The simulated RIXS spectra [DFT-ROCIS($6t_{1u}$)] for $|F1s^{-1}6t_{1u}^1\rangle$ match the polarization dependence measured at 692.7 eV, and the simulated RIXS spectra [DFT-ROCIS($7t_{1u}$)] for $|F1s^{-1}7t_{1u}^1\rangle$ match the polarization dependence measured at 696.3 eV. See Fig. S23 for TD-DFT/CAM-B3LYP simulated RIXS. The blue (dark gray) sticks of intensities for vertical polarization are given a downward shift for clarity and comparison with the orange (light gray) sticks representing the horizontal polarization. The polarization dependence was computed using Eq. (10) in the one-electron picture, neglecting interference between intermediate states. The orange (light gray) spectra indicate spectra at horizontal polarization ($\chi = 0^\circ$), and blue (dark gray) spectra represent vertical polarization ($\chi = 90^\circ$).

prominent as seen for example in the $|F1s^{-1}6a_{1g}^1\rangle$ resonance. This could be due to the fact that the core excitation actually involves both σ and π symmetry t_{1u} orbitals.

Interestingly we find that unlike at the $|F1s^{-1}6a_{1g}^1\rangle$ resonance, TD-DFT/CAM-B3LYP fails to produce the correct polarization dependence for the $7t_{1u}$ resonance, which is correctly predicted by DFT-ROCIS; see Fig. S23. However, the polarization dependence is correctly predicted for the $6t_{1u}$ resonance as shown in Fig. S23. For both resonances, the energy loss predicted by TD-DFT/CAM-B3LYP turns out to be much more accurate.

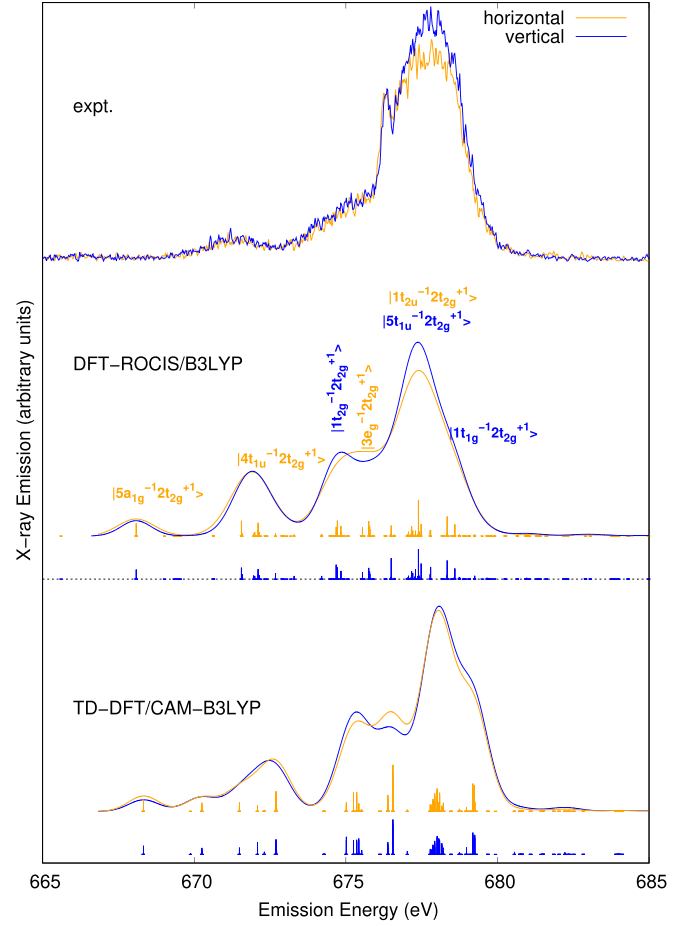


FIG. 8. Simulated polarization-dependent RIXS spectra at DFT-ROCIS/B3LYP and TD-DFT/CAM-B3LYP levels of theory for the $|F1s^{-1}2t_{2g}^1\rangle$ resonance considering a localized core hole, at 699.8 eV and with experimental spectrum obtained from Ref. [13]. The (blue) (dark gray) sticks of intensities for vertical polarization are given a downward shift for clarity and comparison with the orange (light gray) sticks representing the horizontal polarization. The polarization dependence was computed using Eq. (10) in one-electron picture, and neglecting interference between intermediate states. The orange (light gray) spectra indicate horizontal polarization ($\chi = 0^\circ$) and blue (dark gray) spectra represents vertical polarization ($\chi = 90^\circ$).

3. RIXS at the $|F1s^{-1}2t_{2g}^1\rangle$ resonance

For the RIXS at the $|F1s^{-1}2t_{2g}^1\rangle$ resonance, which in experiment was performed after excitation at 699.8 eV, we see that the most intense peak in the spectra has a more intense vertical polarization. This is observed only at the $|F1s^{-1}2t_{2g}^1\rangle$ resonance. In our simulated spectra, we reproduce this feature accurately; see Fig. 8. Unlike in the $|F1s^{-1}6a_{1g}^1\rangle$ resonance we see that here and in all the $|F1s^{-1}t_{1u}^1\rangle$ resonances, the emission originating from $4t_{1u}$ orbital has significant intensity and is prominent. Interestingly, we also see in Figs. 8 and 7 that for RIXS at the $|F1s^{-1}2t_{2g}^1\rangle$ resonance, and to some extent for RIXS at the $|F1s^{-1}6t_{1u}^1\rangle$ resonance, more final states contribute with considerable intensity to the emission spectra. As we see from Fig. 8, there is an additional peak between those of $3e_g$ and $5t_{1u}/1t_{2u}$, which has relatively significant intensity as compared to that in the case of $|F1s^{-1}6a_{1g}^1\rangle$ resonance. This

is indicative of the fact that other states become accessible or allowed as a final state for the $|F1s^{-1}2t_{2g}^1\rangle$ resonance. The increased broadness of the main emission, i.e., peaked around 677.5 eV, for the $|F1s^{-1}2t_{2g}^1\rangle$ resonance, could be due to contributions from these states. These states basically have mixed character with contribution of $5t_{1u}$ and $1t_{2u}$ orbitals and are states generating out of mixing of the $|5t_{1u}^{-1}2t_{2g}^1\rangle$ and $|1t_{2u}^{-1}2t_{2g}^1\rangle$ states. Thus we see that simulations with DFT-ROCIS and with TD-DFT, for the $|F1s^{-1}6a_{1g}^1\rangle$ resonance yield RIXS spectra with all essential features and correct polarization dependence. The polarization dependence generally and more specifically as we see here for a highly symmetrical molecule, like SF_6 , provides insight into the local symmetry of various orbitals and for certain cases provides information on the localization of the orbital on a particular atom. Here we can say beyond the gerade and ungerade symmetry of the states and orbitals, the polarization dependence really characterizes the σ and π symmetry of various MOs with respect to the S-F bond axis aligned to the incident radiation. For example, in the $|F1s^{-1}6t_{1g}^1\rangle$ resonance, the $6a_{1g}$ orbital which always has a σ symmetry with respect to the S-F bond axis, along with the $3e_g$ and $4t_{1u}$ orbitals which also have σ symmetry, are vertically polarized. This is also reflected in the case of the $|F1s^{-1}2t_{2g}^1\rangle$ resonance, where $2t_{2g}$ orbitals having π symmetry with respect to the S-F bonds and similarly orbitals having σ symmetry, i.e., $3e_g$ and $4t_{1u}$ and one of the triply degenerate $1t_{2u}$ have emission with horizontal polarization. As seen also in the case of the $|F1s^{-1}6t_{1u}^1\rangle$ resonances, TD-DFT/CAM-B3LYP fails to predict the correct polarization dependence yet predicts correct energy loss of the peaks in the RIXS spectrum. We find that TD-DFT/CAM-B3LYP follows the same trend for the $|F1s^{-1}2t_{2g}^1\rangle$ resonance; see Fig. 8. We clearly see that DFT-ROCIS predicts a correct polarization dependence, with respect to intensities, for the most intense peak corresponding to the $|1t_{2u}^{-1}2t_{2g}^1\rangle$ and $|5t_{1u}^{-1}2t_{2g}^1\rangle$ states.

D. Role of screening and electron-hole coupling

In Fig. 9 we have reproduced the RIXS spectra from Ekholm *et al.* [13] for $|F1s^{-1}6a_{1g}^1\rangle$, $|F1s^{-1}6/7t_{1u}^1\rangle$ and $|F1s^{-1}2t_{2g}^1\rangle$ XA resonances, along with the XE spectrum. We clearly see from Fig. 9, that the emission energies of RIXS spectra for $|F1s^{-1}6/7t_{1u}^1\rangle$ and $|F1s^{-1}2t_{2g}^1\rangle$ resonances more or less align with the XE spectra. However, for the $|F1s^{-1}6a_{1g}^1\rangle$ resonance RIXS spectra the differences are rather large, and clearly seen from the energy difference in the horizontal portion of the lines of individual colors in Fig. 9. If we for the time being neglect the influence of dynamics, these shifts in emission energy (so-called spectator shifts) can be thought of as a measure of interaction between the hole and particles in the RIXS process, and in other words be described as some sort of descriptor of electron-hole coupling. The reason for observed spectator shift of emission lines is nothing other than the screening of the particular energy levels by the spectator electron. This shift is very sensitive to the spatial distribution of the “spectator” molecular orbital [62].

Interestingly this phenomenon that spectator shifts are significantly more for the $|F1s^{-1}6a_{1g}^1\rangle$ resonances can be easily explained looking at the fact that an electron in the

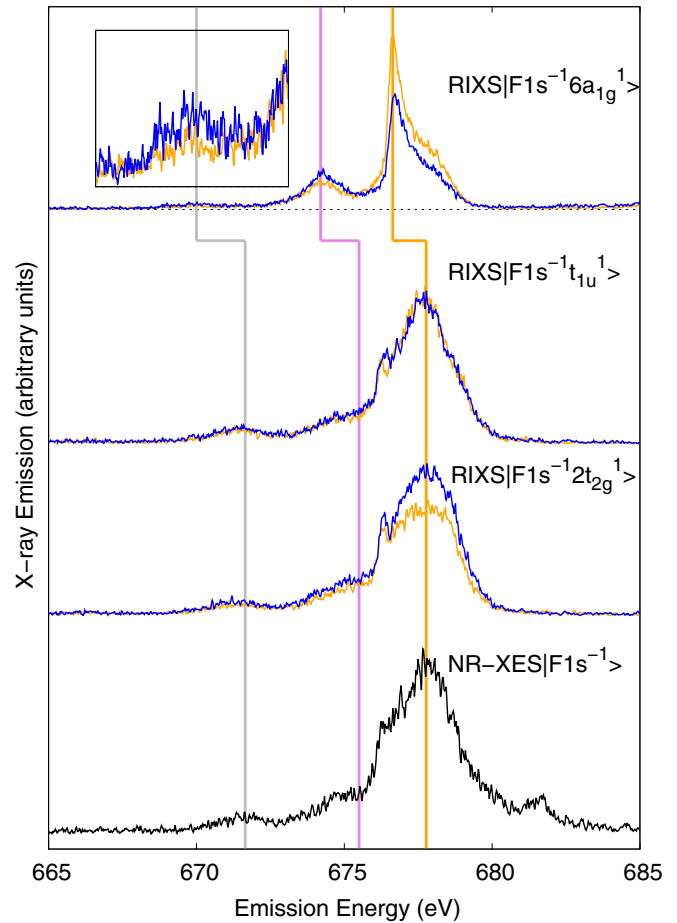


FIG. 9. Comparison of experimentally measured emission spectra obtained at different resonances and nonresonant condition highlighting the spectator shifts. The experimental spectra are reproduced from Ref. [13]. The vertical lines of different colors denote prominent peaks in the emission spectator. Each line of different color bends horizontally, i.e., representing the experimentally observed spectator shift, to align with the resonant emission peak position for the $|F1s^{-1}6a_{1g}^1\rangle$ resonance to the corresponding nonresonant XE peak. The identification or association between the peaks in the $|F1s^{-1}6a_{1g}^1\rangle$ RIXS spectrum and those in the XE spectrum have been motivated from the simulated spectra as shown in Fig. 6 and Fig. S22. The spectator shift for the other resonant peaks are not marked as the shifts are rather small. The red shifts for the orange (first from right), violet (middle), and gray (last from right) lines are 1.13, 1.30, and 1.65 eV, respectively. Compare with Table II for DFT-ROCIS simulated spectator shifts.

$6a_{1g}$ orbital is energetically closest to the hole, hence the electron-hole coupling energy is the largest. Additionally more diffuse orbitals with a smaller charge density will have a less electron-hole coupling energy. The magnitude of electron-hole coupling for a more localized particle (electron) will be greater in magnitude, as a natural consequence of distributed Coulomb interaction. Also to be noted here that $6/7t_{1u}$ have a large diffuse spatial orbital, which also decrease the exciton binding. On the other hand the $2t_{2g}$ orbital is energetically most separated from the hole.

We see from Fig. 9 that the spectator shifts can be measured quantitatively for the most easily identifiable peaks, which

TABLE II. Spectator shifts for emission energies (in eV) from DFT-ROCIS level of theory: Emission energies for RIXS at different $F1s$ resonances, compared to nonresonant XE as obtained from simulation at the DFT-ROCIS level of theory. Valence excitation energies at the DFT-ROCIS level of theory are given in parentheses. We will also give the corresponding nonresonant emission energies.

Resonance Orbital	$ F1s^{-1}6a_{1g}^1\rangle$		$ F1s^{-1}6t_{1u}^1\rangle$		$ F1s^{-1}7t_{1u}^1\rangle$		$ F1s^{-1}2t_{2g}^1\rangle$		XE energy Em.
	Em. (E-Loss)	Shift	Em. (E-Loss)	Shift	Em. (E-Loss)	Shift	Em. (E-Loss)	Shift	
$1t_{1g}^{-1}$	660.45(8.44)	1.61	661.03(13.2)	1.03	661.41(17.43)	0.65	661.24(20.10)	0.82	662.06
$1t_{2u}^{-1}$	658.99(9.90)	1.51	659.65(14.58)	0.85	659.89(18.95)	0.61	660.06(21.28)	0.44	660.50
$5t_{1u}^{-1}$	659.35(9.55)	1.42	659.75(14.48)	1.02	660.15(18.69)	0.62	660.29(21.05)	0.48	660.77
$3e_g^{-1}$	656.90(11.99)	2.04	658.01(16.23)	0.93	658.58(20.26)	0.36	658.66(22.69)	0.28	658.94
$1t_{2g}^{-1}$	657.07(11.83)	1.09	657.42(16.81)	0.74	657.77(21.07)	0.39	657.62(23.73)	0.54	658.16
$4t_{1u}^{-1}$	653.36(15.53)	1.91	655.05(19.19)	0.22	654.92(23.92)	0.35	655.02(26.32)	0.25	655.27
$5a_{1g}^{-1}$	649.42(19.47)	2.00	650.47(23.77)	0.95	651.04(27.80)	0.38	650.988(30.36)	0.43	651.42

are (1) the largest peak associated with $5t_{1u}$ and $1t_{2u}$ orbitals, (2) the low-intensity distinctly separated peaks $1t_{2g}$ and $3e_g$, and (3) the small peak (but identifiable upon magnification, as shown in inset in Fig. 9) associated with the $4t_{1u}$ orbital. The experimental spectator shift for the peak from combined emission from the $5t_{1u}$ and $1t_{2u}$ orbitals was found to be 1.13 eV. We see from Table II, where we tabulate the theoretically computed spectator shifts at the DFT-ROCIS level of theory, and the shift to be 1.51 eV and 1.42 eV for emission from the $5t_{1u}$ and $1t_{2u}$ orbital. However, two of these peaks in the XES and RIXS correspond to a combination of orbitals, ($5t_{1u}$, $1t_{2u}$) and ($1t_{2g}$, $3e_g$) orbitals, and a direct comparison with the theoretically derived spectator shifts for these individual orbitals, at the DFT-ROCIS level of theory, as mentioned in Table II is not totally meaningful. A RIXS experiment with better energy resolution that resolves individual peaks to individual orbitals might be able to more appropriately connect with the values mentioned in Table II.

From Table II we observe an overestimation of computed spectator shift with respect to the experimental spectator shifts. This error is particularly pronounced for the emission for the $|F1s^{-1}6/7t_{1u}^1\rangle$ and $|F1s^{-1}2t_{2g}^1\rangle$ resonances, where the peaks or the emission energies line up with the XE energies. The error is also overestimated for the $|F1s^{-1}6a_{1g}^1\rangle$ resonance. Since the XE spectrum was computed based on an open shell, an $N-1$ electron system with an unrestricted Kohn-Sham SCF protocol from which quasirestricted orbitals were constructed and on the other hand, the RIXS spectra at the DFT-ROCIS level of theory, are computed on N electron systems, using restricted Kohn-Sham SCF orbitals, and there is an overestimation in the simulated spectator shifts.

The emission from $3e_g$ and $1t_{2g}$ overlaps with each other in the RIXS spectra, whereas they are well separated in the XE spectrum by almost ~ 0.8 eV. Experimentally since only one peak for both XE spectrum and $|F1s^{-1}6a_{1g}^1\rangle$ resonance can be identified, for this particular case it should be attributed to an average value between the two emissions. Experimentally this shift turns out to be 1.3 eV. For the simulated spectra the spectator shift for $3e_g$ and $1t_{2g}$ emission turns out to be 2.04 and 1.09, respectively, with the average to be 1.565 eV. For the $4t_{1u}$ emission energies the experimental spectator shift turns out to be 1.65 eV, as compared to the simulated value of 1.91 eV. Interestingly we see that if we consider that there is an error of $\sim 0.38-0.35$ eV in computing the spectator shift,

as demonstrated earlier, then the adjusted value obtained from the simulated spectra for the $|F1s^{-1}6/7t_{1u}^1\rangle$ and $|F1s^{-1}2t_{2g}^1\rangle$ resonances (see Table II) agrees well with experiment, which suggests very small spectator shifts.

E. Dynamical effects in RIXS at the $|F1s^{-1}6a_{1g}^1\rangle$ resonance

The RIXS spectra for the $|F1s^{-1}6a_{1g}^1\rangle$ resonance of SF_6 , at the ground-state equilibrium geometry, has been already simulated the DFT-ROCIS/B3LYP and TD-DFT/CAM-B3LYP levels of theory, as shown in Fig. 6. However, the $F1s$ core excitation gives dramatic changes in the electronic structure and chemical bonding, since according to the equivalent core principle, the valence electrons effectively experience the $F1s^1$ core like that of $Ne1s^2$. Hence, it induces vibrational excitations leading even to dissociative dynamics, which can play a significant role for the RIXS signal [14,29]. For the wave packet dynamics of the RIXS spectrum, the $|F1s^{-1}6a_{1g}^1\rangle$ resonance, we performed a rigid scan along the F_5S-F bond elongation and calculated a one-dimensional cut in the potential energy surfaces of the ground, valence-excited, and core-excited states. The dissociation of the F_5S-F bond transforms the symmetry of the system from O_h to C_{4v} symmetry. Thus, MOs transform accordingly, breaking the inversion symmetry and lifting degeneracy of states. This is seen as a splitting of the one-dimensional cuts in certain degenerate potential energy surfaces. In Table III we show the correlation diagram between the valence-excited states in O_h symmetry and C_{4v} and the splitting of the degenerate states. Notably the triply degenerate states, in O_h symmetry, split into doubly degenerate and single degenerate states, while the doubly degenerate states, in O_h symmetry, split into two singly degenerate states. This gives associated dynamical effects in the RIXS spectrum.

The 1D rigid scan of the F_5S-F dissociation has been carried out with TD-DFT/CAM-B3LYP and DFT-ROCIS/B3LYP. This was done to access the quality of different levels of theory in simulating the valence and core excited states and potential energy surfaces. Since the PES involve SF_5-F bond dissociation, there exists the obvious threat of error being introduced by using single-reference theories, and thus assessment of different theories is warranted.

The adiabatic PES along with highlighted individual diabatic PES are plotted in the Supplemental Material [41]; see

TABLE III. Correlation diagram and splitting of symmetry adapted molecular orbital for along S-F bond elongation for SF₆, i.e. transformation from O_h to C_{4v} symmetry. The bright states are highlighted in bold.

O _h	C _{4v}	Emission energy and (energy loss) at O _h geometry (eV)
$ 1t_{1g}^{-1}6a_{1g}^1\rangle$	$\left\{ \begin{array}{l} e^{-1}a_1^1\rangle \\ a_2^{-1}a_1^1\rangle \end{array} \right.$	660.45 (8.44)
$ 1t_{2u}^{-1}6a_{1g}^1\rangle$	$\left\{ \begin{array}{l} e^{-1}a_1^1\rangle \\ b_1^{-1}a_1^1\rangle \end{array} \right.$	658.99 (9.90)
$ 5t_{1u}^{-1}6a_{1g}^1\rangle$	$\left\{ \begin{array}{l} e^{-1}a_1^1\rangle \\ a_1^{-1}a_1^1\rangle \end{array} \right.$	659.35 (9.55)
$ 3e_g^{-1}6a_{1g}^1\rangle$	$\left\{ \begin{array}{l} a_1^{-1}a_1^1\rangle \\ b_1^{-1}a_1^1\rangle \end{array} \right.$	656.90 (11.99)
$ 1t_{2g}^{-1}6a_{1g}^1\rangle$	$\left\{ \begin{array}{l} e^{-1}a_1^1\rangle \\ b_2^{-1}a_1^1\rangle \end{array} \right.$	657.07 (11.83)
$ 4t_{1u}^{-1}6a_{1g}^1\rangle$	$\left\{ \begin{array}{l} e^{-1}a_1^1\rangle \\ a_1^{-1}a_1^1\rangle \end{array} \right.$	653.36 (15.53)
$ 5a_{1g}^{-1}6a_{1g}^1\rangle$	$\left\{ a_1^{-1}a_1^1\rangle \right.$	649.42 (19.47)

Figs. S6–S14 for DFT-ROCIS and Figs. S16–S21 for TD-DFT/CAM-B3LYP PES.

A comparison between the TD-DFT and DFT-ROCIS diabatic states clearly shows that though there are overall

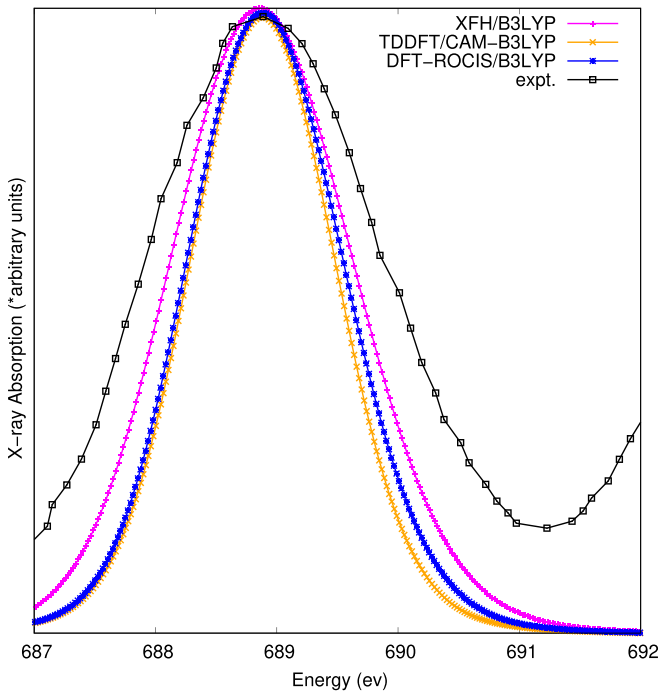


FIG. 10. Vibrational profile of XA peak corresponding to the $|F1s^{-1}6a_{1g}^1\rangle$ state from wave packet simulations using TD-DFT/CAM-B3LYP, DFT-ROCIS/B3LYP, and XFH/B3LYP levels of theory. The experimental spectrum reproduced from Hudson *et al.* [24] is shown for comparison.

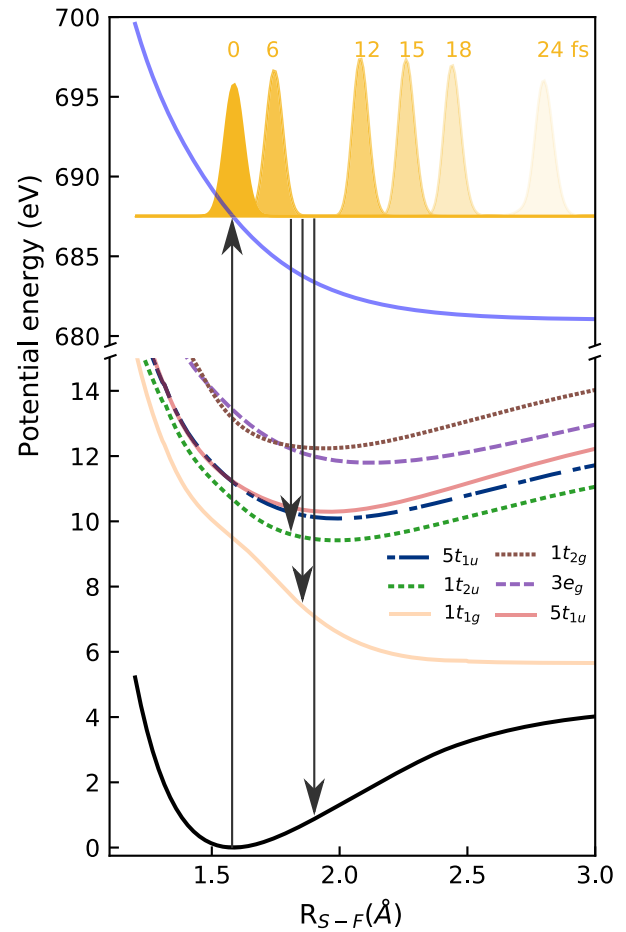


FIG. 11. Wave packet dynamics along the S-F bond dissociation on the XFH/B3LYP $|F1s^{-1}6a_{1g}^1\rangle$ intermediate dissociative state. The ground-state potential energy surface [shown in black (bottom curve)] is shown from which the core excitation takes the wave packet to the $|F1s^{-1}6a_{1g}^1\rangle$ core-excited state [shown in blue (top curve)] on which which the wave packet dynamics occurs. Six valence-excited final states which are considered for the simulation of the dynamical RIXS at the TD-DFT/CAM-B3LYP level of theory, as shown in Fig. 12, into which the decay happens, are shown in different colors (six middle curves) along with the *orbital* labels. The *orbital* ($1t_{1g}$, $1t_{2u}$, $5t_{1u}$, $3e_g$, and $1t_{2g}$) labels correspond to the $|orbital^{-1}6a_{1g}^1\rangle$ states. Decay to the ground-state potential yields quasielastic RIXS.

similarities, the major disagreement comes in the shape of the PES for the $|a_1^{-1}a_1^1\rangle$ state arising from the $|5t_{1u}^{-1}6a_{1g}^1\rangle$ state, when breaking O_h geometry.

While DFT-ROCIS clearly predicts this $|a_1^{-1}a_1^1\rangle$ state to be dissociative (see Fig. S9 [41]), TD-DFT predicts the state to bound; see Fig. S19 [41]. A similar comparison between TD-DFT and DFT-ROCIS for the S₀ ground state and $|F1s^{-1}6a_{1g}^1\rangle$ core-excited state is shown in Fig. S24 [41]. When dynamical effects of the F₅S-F bond dissociation are included, i.e., the vibrational profile of the dissociative $|F1s^{-1}6a_{1g}^1\rangle$ state is included in the absorption spectra, we clearly see that the DFT-ROCIS and TD-DFT core-excited PES fail to produce the experimental broadness of the XA spectrum. This could be due to two reasons: (1) in the one-dimensional cuts in the PES for DFT-ROCIS and TD-DFT, the curves are too shallow

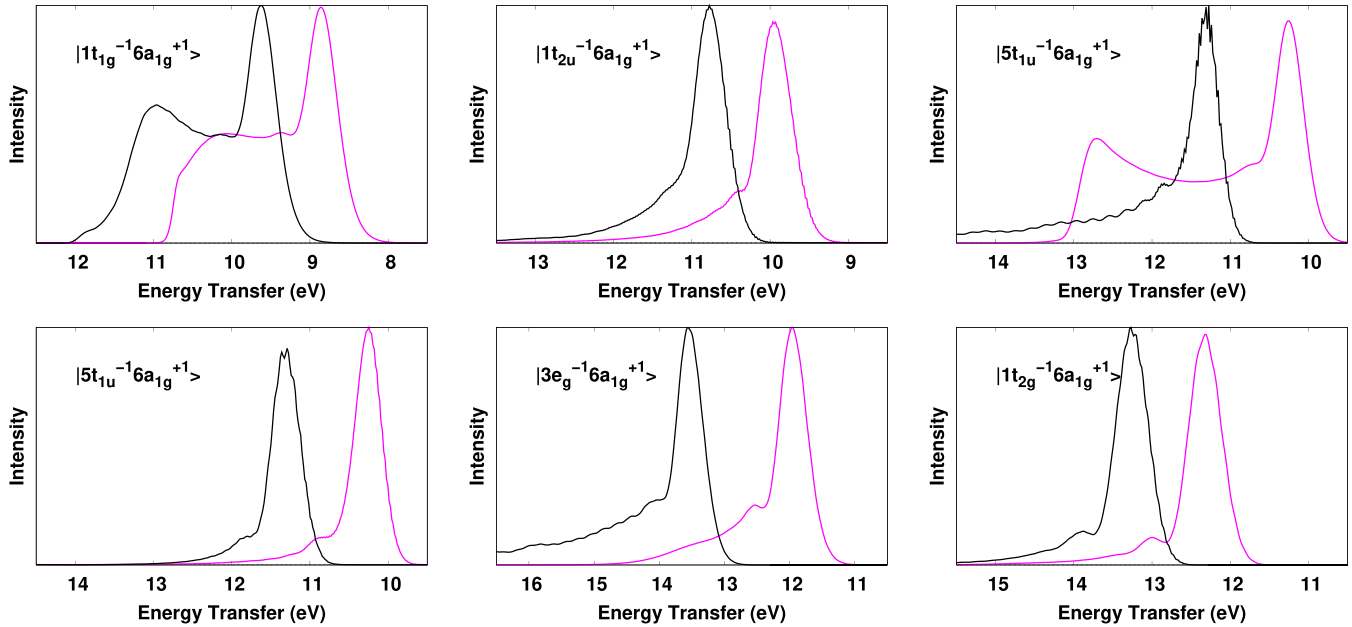


FIG. 12. Role of nuclear dynamics on the RIXS via the $|F1s^{-1}6a_{1g}^1\rangle$ dissociative core-excited state to the final states $|1t_{1g}^{-1}6a_{1g}^1\rangle$, $|1t_{2u}^{-1}6a_{1g}^1\rangle$, $|5t_{1u}^{-1}6a_{1g}^1\rangle$, $|3e_g^{-1}6a_{1g}^1\rangle$, and $|1t_{2g}^{-1}6a_{1g}^1\rangle$. It is important to notice that RIXS to the symmetry-forbidden ungerade final states $|1t_{2u}^{-1}6a_{1g}^1\rangle$ and $|5t_{1u}^{-1}6a_{1g}^1\rangle$ are allowed only due to the vibronic coupling which localizes the core hole on the *F* atom. Black and magenta (gray) show TD-DFT/CAM-B3LYP and DFT-ROCIS/B3LYP calculations, respectively. The state labels refer to orbital assignment at the equilibrium geometry and for stating splitting from O_h to C_{4v} symmetry presented in Table III.

and (2) the absence of other nuclear degrees of freedom. As discussed earlier in Methods Sec. II, the model essentially constitutes of the only SF₅-F bond dissociation and other angular distortion modes are neglected. The steepness of the core excited states can also be strongly affected by the neglect of these other degrees of freedom, which would result in underestimation of the broadening of the XA spectrum. The methods which we employ here like TD-DFT and DFT-ROCIS lack proper accounting of the core-hole relaxation effects, which in turn could change the intermediate state PES.

It is well known that orbital relaxation effects play an important role in the core-excited states and is a potential cause for the absence of the desired steepness. Full-core-hole excited (XFH) giving a relaxation of the lowest core-excited state (within the constraint of the core-valence separation approximation) is known to capture these orbital relaxation effects [33]. Indeed, the XFH method manages to produce a steeper potential for the $|F1s^{-1}6a_{1g}^1\rangle$ state than the TD-DFT and DFT-ROCIS; see Fig. S24. We also see that when the XFH potential energy cut is used to compute the vibrational profile of the XA spectrum, a broader spectrum is achieved though it still fails to match the experimental broadness; see Fig. 10. Hence the $|F1s^{-1}6a_{1g}^1\rangle$ core-excited state computed with the XFH is used for computing the dynamical effects of F₅S-F bond dissociation on the RIXS spectra, with both DFT-ROCIS and TD-DFT valence-excited states. Emission along the vertical polarization was found to be twice the horizontal polarization for the elastic line, which is reflected in the vibrational tail in the experimental spectrum at energies lower than 687 eV.

Thus we conducted the wave packet dynamics on the XFH/B3LYP intermediate (core-excited) state along the

F₅S-F bond-dissociation distance (see Fig. 11) along with the final (valence-excited) state obtained from DFT-ROCIS/B3LYP and TD-DFT/CAM-B3LYP. The vibrational profiles for the different individual peaks arising out of transition from the $|F1s^{-1}6a_{1g}^1\rangle$ intermediate state and the individual final states of different symmetry, as listed in Table III, were computed individually with a distance-dependent transition-dipole moment, as shown in Fig. 12.

Due to the localization of the core hole and dissociation along a single S-F bond, the symmetry of molecule is reduced from O_h to C_{4v} and the states $|1t_{1g}^{-1}6a_{1g}^1\rangle$, $|1t_{2u}^{-1}6a_{1g}^1\rangle$, $|5t_{2u}^{-1}6a_{1g}^1\rangle$ and $|1t_{2g}^{-1}6a_{1g}^1\rangle$ split into a-states and double degenerate e-states. This means that triply degenerate states mentioned above in O_h symmetry have split into PESs along S-F bond elongation, which correspond to a doubly degenerate e state and a $a_1/a_2/b_1/b_2$ state in C_{4v} symmetry. According to our simulations only the e-states in C_{4v} symmetry, associated with $|1t_{1g}^{-1}6a_{1g}^1\rangle$, $|1t_{2u}^{-1}6a_{1g}^1\rangle$, $|1t_{2g}^{-1}6a_{1g}^1\rangle$ states in O_h symmetry, are active (bright), and hence in Fig. 12 we include only spectra simulated for PESs of the bright e-states. In contrast, in the case of the $|5t_{2u}^{-1}6a_{1g}^1\rangle$ state, all three states (e and a_1) are active (bright). Therefore we display in Fig. 12 spectra associated with the bright e- and a_1 -states.

As it can be seen in Fig. 12, the dissociative wave packet dynamics in the core-excited state leads to a strong distortion of the line shapes of the final electronic states populated in the RIXS process. Moreover, the results are very sensitive on the choice of theoretical methodology used to compute the potential energy curves, as discussed above. The most striking difference occurs in the profile for decay to the analogously dissociative pair of $1t_{1g}$ final states, wherein a splitting is

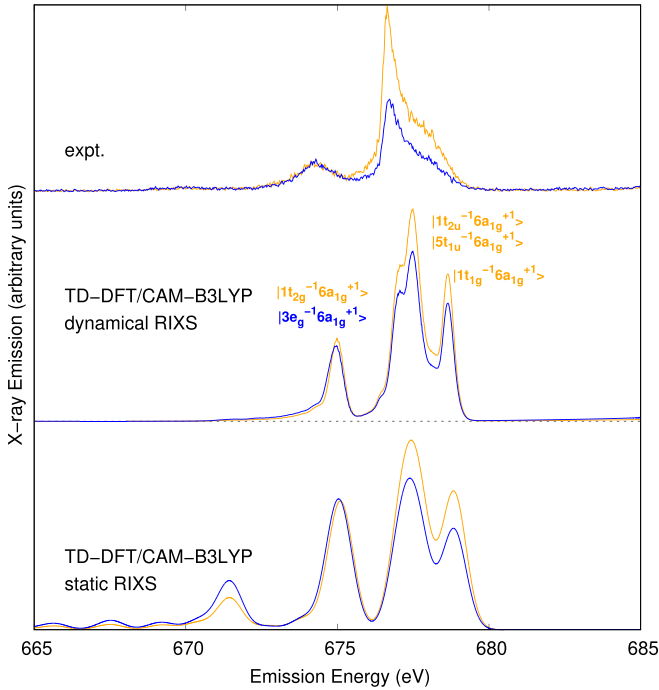


FIG. 13. Role of the nuclear dynamics. Experimental and calculated quasielastic RIXS bands for horizontal [orange (light gray)] and vertical [blue (dark gray)] photon polarization along with experimental spectrum obtained from Ref. [13]. Mid- and lower panels compare total theoretical RIXS profile with and without taking into account the nuclear dynamics, respectively. The peaks corresponding to $|4t_{1u}^{-1}6a_{1g}^1\rangle$ and $|5a_{1g}^{-1}6a_{1g}^1\rangle$ are not present in the dynamical spectra, as those states could not be diabaticized properly and are hence omitted from simulations. The static spectrum is convoluted by a constant Gaussian broadening whereas the broadening in the dynamical spectra results from the wave packet dynamics.

observed, typical for decay between two dissociative curves [14,15] arising from fast decay near the vertical point and decay from stretched bond geometries. Decay from the wave packet in a stretched S-F bond leads to second peak located at higher energy losses than fast decay near the vertical point.

The scenario outlined above has an important consequence. When considering the experimental RIXS spectrum at the a_{1g} resonance it was observed a sharp feature [13] associated with dissociation of the S-F bond. The wave packet simulations support this notion, only that it seems to happen indirectly, explicitly the higher loss shoulder of the $1t_{1g}$ bands overlaps with the profile of the $1t_{2u}$ states, leading to increased intensity in the spectral region of the latter state. The discussed effect is shown in Fig. 13 and Fig. S25. The $|4t_{1u}^{-1}6a_{1g}^1\rangle$ and $|5a_{1g}^{-1}6a_{1g}^1\rangle$ states are not present in the TD-DFT dynamical spectra, due to inability to correctly diabaticize those states. However, at the DFT-ROCIS level of theory the $|4t_{1u}^{-1}6a_{1g}^1\rangle$ state could be diabaticized and included in the dynamical spectrum simulation at the DFT-ROCIS level of theory as shown in Fig. S25. Interestingly the peak associated with $|4t_{1u}^{-1}6a_{1g}^1\rangle$ state is suppressed due to the dissociative dynamics, as shown in Fig. S26, and hence the model employed for dynamical simulations also holds at lower emission energy as well.

The dissociation in the core-excited SF_6 molecule additionally leads to low-energy losses near the elastic line. These are associated with population of the vibrational levels in the ground-state potential energy surface. Figure S27 shows a comparison between experimental and calculated RIXS spectra for vertical and horizontal polarization. It can be seen that the experimental band is asymmetric and extends for about 4.5 eV. However, no vibrational peaks can be distinguished, as experimental resolution is limited. The theoretical RIXS spectrum, computed within a one-dimensional wave packet model, evidences a long progression of vibrational states associated with the S-F stretching vibration. We expect that future high-resolution measurements could resolve this progression, but it should also be considered that additional vibrational modes not included in our simulations could lead to additional peaks.

IV. CONCLUSION

To conclude, the electronic structure and nuclear dynamics of the SF_6 molecule have been investigated with F1s XA and RIXS spectroscopy and analyzed using first-principle electronic calculations accompanied by the wave packet simulations of the nuclear dynamics. In the simulations, we employ two levels of quantum chemical methods: TD-DFT/CAM-B3LYP and DFT-ROCIS/B3LYP. Due to the strong degeneracy of the F1s core shell in SF_6 , the vibronic coupling results in a localization of the core hole in the F atom. The core-hole localization and associated elongation of the corresponding S-F bond reduce the symmetry from O_h to C_{4v} . This results in a drastic change of the symmetry selection rules, as seen in the experimental RIXS spectrum. For example, RIXS through the core-excited state $|F1s^{-1}6a_{1g}^1\rangle$ to the symmetry-forbidden scattering channels in the ungerade final states $|1t_{2u}^{-1}6a_{1g}^1\rangle$ and $|5t_{1u}^{-1}6a_{1g}^1\rangle$ becomes allowed due to the vibronic coupling.

Our simulations are in agreement with the experiment and explain the sensitivity of the RIXS spectra to the symmetry of the XA resonance by different screening or electron-hole interaction. We have shown that the so-called spectator shift of the RIXS spectra is larger for the $|F1s^{-1}6a_{1g}^1\rangle$ resonance than for the $|F1s^{-1}6t_{1u}^1\rangle$, $|F1s^{-1}7t_{1u}^1\rangle$, and $|F1s^{-1}2t_{2g}^1\rangle$ XA resonances. The reason for this is that the $6a_{1g}$ orbital gives an efficient screening of the core hole since it is largely localized on the F atoms. Hence, there is a large spectator shift for the $|F1s^{-1}6a_{1g}^1\rangle$ resonance.

For comparison to the experimental data, we calculated the RIXS profile for two angles χ between the polarization vector \vec{e} of incoming photon and momentum \vec{k}' of scattered photon, $\chi = 0^\circ$ and 90° . Our theoretical results explain observed polarization dependence of the experimental RIXS profile by its dependence on the mutual orientation of the dipole moments of core-excitation and emission transitions. Nuclear dynamics influences both electronically inelastic and elastic RIXS channels. Most strongly the nuclear dynamics affects the quasielastic RIXS channel through the dissociative intermediate $|F1s^{-1}6a_{1g}^1\rangle$ state with a long vibrational progression.

The data sets generated and analyzed during the current study are available from the corresponding author on reasonable request.

ACKNOWLEDGMENTS

M.O. acknowledges funding from the European Union's Horizon 2020 research and innovation program under the Marie Skłodowska-Curie Grant Agreement No. 860553 and the Swedish Research Council (VR Contract No. 2021-04521). A.B. and M.O. acknowledge funding from the Carl Tryggers Foundation (Contract No. CTS18:285). The calculations were enabled by resources provided by the Swedish National Infrastructure for Computing (SNIC) at the Swedish National Supercomputer Center (NSC), the High Performance Computer Center North (HPC2N), and

the Chalmers Centre for Computational Science and Engineering (C3SE) partially funded by the Swedish Research Council through Grant Agreement No. 2018-05973. J.-E. R. acknowledges support from the Swedish Research Council (VR Contract No. 2021-04017). The authors declare no competing financial or nonfinancial interests.

The project was designed and led by A.B., V.V.C., F.G., and M.O. Simulations were performed and analyzed by A.B. and V.V.C. The manuscript was written by A.B., V.V.C., and M.O. All authors contributed to the manuscript. Correspondence and requests for materials should be addressed to M.O.

-
- [1] F. de Groot, *Chem. Rev.* **101**, 1779 (2001).
- [2] P. Norman, K. Ruud, and T. Saue, *Principles and Practices of Molecular Properties: Theory, Modeling, and Simulations* (Wiley, Chichester, UK, 2018).
- [3] J. Nordgren and J.-E. Rubensson, *J. Electron Spectrosc. Relat. Phenom.* **188**, 3 (2013).
- [4] M. Simon and T. Schmitt, *J. Electron Spectrosc. Relat. Phenom.* **188**, 1 (2013).
- [5] L. J. P. Ament, M. van Veenendaal, T. P. Devereaux, J. P. Hill, and J. van den Brink, *Rev. Mod. Phys.* **83**, 705 (2011).
- [6] F. Gel'mukhanov, M. Odellius, S. P. Polyutov, A. Föhlisch, and V. Kimberg, *Rev. Mod. Phys.* **93**, 035001 (2021).
- [7] M. Beye, P. Wernet, C. Schüßler-Langeheine, and A. Föhlisch, *J. Electron Spectrosc. Relat. Phenom.* **188**, 172 (2013).
- [8] J.-P. Rueff and A. Shukla, *Rev. Mod. Phys.* **82**, 847 (2010).
- [9] J.-E. Rubensson, *J. Electron Spectrosc. Relat. Phenom.* **110-111**, 135 (2000).
- [10] K. D. Nanda and A. I. Krylov, *J. Chem. Phys.* **152**, 244118 (2020).
- [11] T. Marchenko, S. Carniato, L. Journal, R. Guillemin, E. Kawerk, M. Žitnik, M. Kavčič, K. Bučar, R. Bohinc, M. Petric *et al.*, *Phys. Rev. X* **5**, 031021 (2015).
- [12] A. Santos, O. Travnikova, N. Boudjemia, T. Marchenko, R. Guillemin, I. Ismail, D. Koulentianos, D. Céolin, F. Gel'mukhanov, M. Simon *et al.*, *J. Vac. Sci. Technol. A* **40**, 042801 (2022).
- [13] V. Ekholm, G. S. Chiužbăian, C. Sâthe, A. Nicolaou, M. Guarise, M. Simon, N. Jaouen, J. M. Lüning, C. F. Hague, F. K. H. Gel'mukhanov *et al.*, *J. Phys. B: At. Mol. Opt. Phys.* **53**, 185101 (2020).
- [14] E. Ertan, V. Savchenko, N. Ignatova, V. Vaz da Cruz, R. C. Couto, S. Eckert, M. Fondell, M. Dantz, B. Kennedy, T. Schmitt *et al.*, *Phys. Chem. Chem. Phys.* **20**, 14384 (2018).
- [15] V. Vaz da Cruz, N. Ignatova, R. C. Couto, D. A. Fedotov, D. R. Rehn, V. Savchenko, P. Norman, H. Ågren, S. Polyutov, J. Niskanen *et al.*, *J. Chem. Phys.* **150**, 234301 (2019).
- [16] S. Eckert, V. V. da Cruz, F. Gel'mukhanov, E. Ertan, N. Ignatova, S. Polyutov, R. C. Couto, M. Fondell, M. Dantz, B. Kennedy *et al.*, *Phys. Rev. A* **97**, 053410 (2018).
- [17] R. C. Couto, V. V. Cruz, E. Ertan, S. Eckert, M. Fondell, M. Dantz, B. Kennedy, T. Schmitt, A. Pietzsch, F. F. Guimarães *et al.*, *Nat. Commun.* **8**, 14165 (2017).
- [18] F. Kh. Gel'mukhanov, L. N. Mazalov, and N. A. Shklyaveva, *Zh. Eksp. Teor. Fiz.* **69**, 1971 (1975) [*Sov. Phys. JETP* **42**, 1001 (1975)].
- [19] L. Argenti, T. D. Thomas, E. Plésiat, X. Liu, C. Miron, T. Lischke, G. Prümper, K. Sakai, T. Ouchi, R. Püttner *et al.*, *New J. Phys.* **14**, 033012 (2012).
- [20] X.-J. Liu, Q. Miao, F. Gel'mukhanov, M. Patanen, O. Travnikova, C. Nicolas, H. Ågren, K. Ueda, and C. Miron, *Nat. Photonics* **9**, 120 (2015).
- [21] L. Cederbaum and F. Tarantelli, *J. Chem. Phys.* **99**, 5871 (1993).
- [22] P. Skytt, P. Glans, J.-H. Guo, K. Gunnelin, C. Sâthe, J. Nordgren, F. K. Gel'mukhanov, A. Cesar, and H. Ågren, *Phys. Rev. Lett.* **77**, 5035 (1996).
- [23] F. Gel'mukhanov, T. Privalov, and H. Ågren, *J. Exp. Theor. Phys.* **85**, 20 (1997).
- [24] E. Hudson, D. A. Shirley, M. Domke, G. Remmers, A. Puschmann, T. Mandel, C. Xue, and G. Kaindl, *Phys. Rev. A* **47**, 361 (1993).
- [25] Y. Pertot, C. Schmidt, M. Matthews, A. Chauvet, M. Huppert, V. Svoboda, A. Von Conta, A. Tehlar, D. Baykusheva, J.-P. Wolf, and H. J. Wörner, *Science* **355**, 264 (2017).
- [26] P. Rupprecht, L. Aufleger, A. Magunia, S. Heinze, T. Ding, M. Rebholz, S. Amberg, N. Mollov, F. Henrich, M. Haverkort, C. Ott, and T. Pfeifer, in *International Conference on Ultrafast Phenomena* (Optica Publishing Group, 2020), pp. Th3B–2.
- [27] L. Barreau, A. D. Ross, V. Kimberg, P. Krasnov, S. Blinov, D. M. Neumark, and S. R. Leone, *Phys. Rev. A* **108**, 012805 (2023).
- [28] O. Travnikova, J.-C. Liu, A. Lindblad, C. Nicolas, J. Söderström, V. Kimberg, F. Gel'mukhanov, and C. Miron, *Phys. Rev. Lett.* **105**, 233001 (2010).
- [29] O. Björneholm, S. Sundin, S. Svensson, R. R. T. Marinho, A. N. Naves de Brito, F. Gel'mukhanov, and H. Ågren, *Phys. Rev. Lett.* **79**, 3150 (1997).
- [30] F. Neese, F. Wennmohs, U. Becker, and C. Riplinger, *J. Chem. Phys.* **152**, 224108 (2020).
- [31] M. Roemelt, D. Maganas, S. DeBeer, and F. Neese, *J. Chem. Phys.* **138**, 204101 (2013).
- [32] M. A. Marques and E. K. Gross, *Annu. Rev. Phys. Chem.* **55**, 427 (2004).
- [33] M. Iannuzzi and J. Hutter, *Phys. Chem. Chem. Phys.* **9**, 1599 (2007).
- [34] J. Hutter, M. Iannuzzi, F. Schiffmann, and J. VandeVondele, *WIREs Comput. Mol. Sci.* **4**, 15 (2014).
- [35] M. J. Frisch, G. W. Trucks, H. B. Schlegel, G. E. Scuseria, M. A. Robb, J. R. Cheeseman, G. Scalmani, V. Barone, G. A. Petersson, H. Nakatsuji *et al.*, Gaussian 16 Revision C.01 (Gaussian Inc., Wallingford CT, 2016).

- [36] Y. Zhao and D. G. Truhlar, *Theor. Chem. Acc.* **120**, 215 (2008).
- [37] E. E. Dahlke, R. M. Olson, H. R. Leverentz, and D. G. Truhlar, *J. Phys. Chem. A* **112**, 3976 (2008).
- [38] F. Weigend and R. Ahlrichs, *Phys. Chem. Chem. Phys.* **7**, 3297 (2005).
- [39] K. Kuchitsu, *Structure of Free Polyatomic Molecules: Basic Data* (Springer Science & Business Media, Berlin, Heidelberg, 2013).
- [40] G. Herzberg, *Molecular Spectra and Molecular Structure* (D. Van Nostrand, New York, 1945).
- [41] See Supplemental Material at <http://link.aps.org/supplemental/10.1103/PhysRevA.108.023103> for additional figures of molecular orbitals, S-F bond dissociation dynamics for $|F1s^{-1}6a_{1g}^1\rangle$ state, NR-XES spectrum, PES for valence excited and core-excited states, RIXS spectra, etc.
- [42] M. O. Krause, *J. Phys. Chem. Ref. Data* **8**, 307 (1979).
- [43] B. Schimmelpfennig, B. Nestmann, and S. Peyerimhoff, *J. Electron Spectrosc. Relat. Phenom.* **74**, 173 (1995).
- [44] Y. Gao, T. Tiedje, P. C. Wong, and K. A. R. Mitchell, *Phys. Rev. B* **48**, 15578 (1993).
- [45] R. A. Ingle, A. Banerjee, C. Bacellar, T. R. Barillot, L. Longetti, M. Coreno, M. de Simone, F. Zuccaro, L. Poletto, P. Miotti *et al.*, *J. Phys. B: At. Mol. Opt. Phys.* **55**, 044001 (2022).
- [46] H. A. Kramers and W. Heisenberg, *Z. Phys.* **31**, 681 (1925).
- [47] J. Foster and S. Boys, *Rev. Mod. Phys.* **32**, 300 (1960).
- [48] F. Gel'mukhanov and H. Ågren, *Phys. Rev. A* **49**, 4378 (1994).
- [49] S. Kossmann and F. Neese, *Chem. Phys. Lett.* **481**, 240 (2009).
- [50] V. V. da Cruz, S. Eckert, and A. Föhlisch, *Phys. Chem. Chem. Phys.* **23**, 1835 (2021).
- [51] P. Norman and A. Dreuw, *Chem. Rev.* **118**, 7208 (2018).
- [52] T. Yanai, D. P. Tew, and N. C. Handy, *Chem. Phys. Lett.* **393**, 51 (2004).
- [53] R. Izsák and F. Neese, *J. Chem. Phys.* **135**, 144105 (2011).
- [54] A. L. Fetter and J. D. Walecka, *Quantum Theory of Many-Particle Systems* (Courier Corporation, New York, 2012).
- [55] G. J. Martyna and M. E. Tuckerman, *J. Chem. Phys.* **110**, 2810 (1999).
- [56] V. Vaz da Cruz, E. Ertan, R. C. Couto, S. Eckert, M. Fondell, M. Dantz, B. Kennedy, T. Schmitt, A. Pietzsch, F. F. Guimarães *et al.*, *Phys. Chem. Chem. Phys.* **19**, 19573 (2017).
- [57] M. Kadek, L. Konecny, B. Gao, M. Repisky, and K. Ruud, *Phys. Chem. Chem. Phys.* **17**, 22566 (2015).
- [58] R. Martin, S. Kowalczyk, and D. Shirley, *J. Chem. Phys.* **68**, 3829 (1978).
- [59] H. Ågren, R. Arneberg, J. Müller, and R. Manne, *Chem. Phys.* **83**, 53 (1984).
- [60] D. Maganas, P. Kristiansen, L.-C. Duda, A. Knop-Gericke, S. DeBeer, R. Schlögl, and F. Neese, *J. Phys. Chem. C* **118**, 20163 (2014).
- [61] S. Eckert, V. Vaz da Cruz, M. Ochmann, I. von Ahnen, A. Föhlisch, and N. Huse, *J. Phys. Chem. Lett.* **12**, 8637 (2021).
- [62] P. Skytt, P. Glans, K. Gunnelin, J. Guo, J. Nordgren, Y. Luo, and H. Ågren, *Phys. Rev. A* **55**, 134 (1997).